Bayesian model comparison and analysis of the Galactic disc population of gamma-ray millisecond pulsars

Bartels, R.T.; Edwards, T.D.P.; Weniger, C.

DOI
10.1093/mnras/sty2529

Publication date
2018

Document Version
Final published version

Published in
Monthly Notices of the Royal Astronomical Society

Monthly Notices of the ROYAL ASTRONOMICAL SOCIETY

MNRAS **481,** 3966–3987 (2018)
Advance Access publication 2018 September 14

doi:10.1093/mnras/sty2529

Bayesian model comparison and analysis of the Galactic disc population of gamma-ray millisecond pulsars

R. T. Bartels,★ T. D. P. Edwards★ and C. Weniger★

Gravitation Astroparticle Physics Amsterdam (GRAPPA), Institute for Theoretical Physics Amsterdam and Delta Institute for Theoretical Physics, University of Amsterdam, Science Park 904, NL-1098 XH Amsterdam, the Netherlands

Accepted 2018 September 13. Received 2018 August 24; in original form 2018 June 5

ABSTRACT

Pulsed emission from almost one hundred millisecond pulsars (MSPs) has been detected in γ-rays by the *Fermi* Large-Area Telescope. The global properties of this population remain relatively unconstrained despite many attempts to model their spatial and luminosity distributions. We perform here a self-consistent Bayesian analysis of both the spatial distribution and luminosity function simultaneously. Distance uncertainties, arising from errors in the parallax measurement or Galactic electron-density model, are marginalized over. We provide a public PYTHON package (available from http://github.com/tedwards2412/MSPDist) for calculating distance uncertainties to pulsars derived using the dispersion measure by accounting for the uncertainties in Galactic electron-density model YMW16. Finally, we use multiple parametrizations for the MSP population and perform Bayesian model comparison, finding that a broken power-law luminosity function with Lorimer spatial profile are preferred over multiple other parametrizations used in the past. The best-fitting spatial distribution and number of γ-ray MSPs is consistent with results for the radio population of MSPs.

Key words: pulsars: general – Galaxy: disc – gamma-rays: general.

1 INTRODUCTION

Millisecond pulsars (MSPs) are believed to be recycled pulsars that are spun-up to millisecond periods by accreting matter from a companion star (Bhattacharya & van den Heuvel 1991). Prior to the launch of the *Fermi* Gamma-Ray Space Telescope pulsations from only one MSP had been claimed in γ-rays and at low statistical significance (Kuiper et al. 2000). Since then the Large Area Telescope (LAT) aboard *Fermi* has revolutionized the field with close to one hundred γ-ray detected MSPs (Abdo et al. 2009a,b, 2013; Caraveo 2014). Most detections of γ-ray pulsations in MSPs follow from phase-folding the timing parameters already known from radio (e.g. Abdo et al. 2009a). In many cases, the radio MSPs have been initially detected during follow-up observations of *Fermi* unassociated sources after which the timing information is utilized to confirm γ-ray pulsations (e.g. Cognard et al. 2011). Increased computing power has made it possible to detect γ-ray pulsations in blind searches where no timing information is available (Pletsch et al. 2012; Clark et al. 2018).

Population studies of MSPs in radio have constrained their spatial distribution, luminosity function, and the number of radio-emitting MSPs in the Galactic disc (Cordes & Chernoff 1997; Lyne et al. 1998; Levin et al. 2013). On the other hand, γ-ray population studies of MSPs have been performed to constrain their luminosity function and in some cases their spatial distribution (Grégoire & Knödlseder 2013; Hooper et al. 2013; Cholis, Hooper & Linden 2014; Yuan & Zhang 2014; Hooper & Mohlabeng 2016; Winter et al. 2016; Ploeg et al. 2017).

A particular goal of many of these analyses has been to rule-out or constrain the MSP interpretation of the *Fermi* Galactic Center Excess (GCE). The GCE is an excess of γ-rays at energies of $\sim$2 GeV that is spatially coincident with the Galactic Bulge (Goodenough & Hooper 2009; Calore, Cholis & Weniger 2015; Daylan et al. 2016), and was also shown to be morphologically similar (Bartels et al. 2018). It has been suggested that the GCE could be caused by a bulge population of MSPs (Abazajian 2011; Gordon & Macias 2013). Corroborative evidence for this scenario was found by analysing the photon statistics of the inner-Galaxy (Bartels, Krishnamurthy & Weniger 2016; Lee et al. 2016). However, arguments against this scenario exist based on an apparent conflict between the luminosity function of MSPs in the Galactic disc and the intensity of the GCE. It was argued that if the GCE is caused by MSPs we should have already detected a few dozen sources from this population (Hooper et al. 2013; Cholis et al. 2014; Hooper & Mohlabeng 2016). Conversely, other studies claimed that there is no discrepancy if bulge MSPs have the same luminosity function as disc MSPs (Yuan & Zhang 2014; Petrović, Serpico & Zaharijas 2015; Ploeg et al. 2017). Previous analyses have used a variety of distributions for the luminosity function of MSPs. Moreover, they

★ E-mail: r.t.bartels@uva.nl (R.T.B.); t.d.p.edwards@uva.nl (T.D.P.E.); c.weniger@uva.nl (C.W.)

have used different treatments of the distance estimates to MSPs, which is one of the major sources of uncertainty when estimating the pulsar luminosity. In the light of conflicting conclusions caused by particular assumptions it seems important to perform a complete and unbiased analysis, presenting all sources of uncertainty clearly and adopting a conservative set of assumptions.

In this work we perform systematic and fully self-consistent analyses of the spatial distribution and luminosity function of MSPs. We consider different luminosity functions and parametrizations of the spatial profile, performing a Bayesian-unbinned likelihood analysis to constrain the model parameters. Bayesian model comparison is then applied to select the best model. In our analysis we marginalize over the main sources of uncertainty, namely the distance to and received flux of each source. What is more, to the best of our knowledge, we for the first time construct probability distribution functions for distances derived from the dispersion measure (DM) by taking into account the uncertainties in the parameters of the electron-density models (Yao, Manchester & Wang 2017). Finally, we also study how the inclusion of unassociated sources can impact our results.

The layout of the paper is as follows. We first discuss our modelling and MSP data sample in Section 2. Results are then given in Section 3. Finally we discuss the implications of our results in Section 4 and conclude in Section 5.

2 METHODOLOGY AND DATA

In this work we perform a Bayesian-unbinned likelihood analysis in order to fully exploit the heterogeneous information available in the data sample. We first discuss the likelihood function and then address the two main areas of uncertainty, namely the distances to sources and the contribution from unassociated sources.

2.1 Likelihood

Our analysis is based on an unbinned Poisson likelihood function,

$$\mathcal{L}(\mathcal{D}|\boldsymbol{\Theta}) = \mathrm{e}^{-\mu(\boldsymbol{\Theta})} \prod_{i}^{N_{\rm obs}} N_{\rm tot} P(\mathcal{D}_i|\boldsymbol{\Theta}), \tag{1}$$

where $\boldsymbol{\Theta}$ is the vector of parameter dependencies, $N_{\rm obs}$ is the number of observed MSPs, $N_{\rm tot}$ the total number of sources and $P(\mathcal{D}_i|\boldsymbol{\Theta})$ is the probability of finding a given source at Galactic position (ℓ_i, b_i), with observed flux F_i and, if available, parallax or DM ω_i or DM$_i$, i.e. $\mathcal{D}_i = \{\ell_i, b_i, F_i, \kappa_i\}$ with $\kappa_i = \omega_i$ if a parallax measurement is present, or else $\kappa_i = \mathrm{DM}_i$ if a DM measurement exists. If no distance measure is present $\mathcal{D}_i = \{\ell_i, b_i, F_i\}$. Furthermore, $\mu(\boldsymbol{\Theta})$ is the expected number of observed sources and satisfies in the point of maximum likelihood the condition

$$\mu(\boldsymbol{\Theta}_{\rm bf}) = N_{\rm obs}\ , \tag{2}$$

where $\boldsymbol{\Theta}_{\rm bf}$ are the maximum-likelihood values for the parameters of our model. More specifically, $\mu(\boldsymbol{\Theta})$ and $P(\mathcal{D}_i|\boldsymbol{\Theta})$ are given by

$$\begin{aligned}\mu(\boldsymbol{\Theta}) = N_{\rm tot} \sum_{j=1}^{N_{\rm pix}} \frac{\Omega_j}{\cos b_j} \int \mathrm{d}D \int \mathrm{d}L\ P(L|\boldsymbol{\Theta}) \\ \times P(\ell_j, b_j, D|\boldsymbol{\Theta}) \\ \times P_{\rm th}\left(\frac{L}{4\pi D^2}\middle|\boldsymbol{\Theta}, \ell_j, b_j\right),\end{aligned} \tag{3}$$

$$\begin{aligned}P(\ell_i, b_i, F_i, \kappa_i|\boldsymbol{\Theta}) = 4\pi \int \mathrm{d}D \int \mathrm{d}F\ D^2 P(\ell_i, b_i, D|\boldsymbol{\Theta}) \\ \times P\left(L = 4\pi D^2 F|\boldsymbol{\Theta}\right) P_{\rm th}\left(F|\,\boldsymbol{\Theta}, \ell_i, b_i\right) \\ \times P(\kappa_i|D) P(F_i|F)\end{aligned} \tag{4a}$$

$$\begin{aligned}P(\ell_i, b_i, F_i|\boldsymbol{\Theta}) = 4\pi \int \mathrm{d}D \int \mathrm{d}F\ D^2 P(\ell_i, b_i, D|\boldsymbol{\Theta}) \\ \times P\left(L = 4\pi D^2 F|\boldsymbol{\Theta}\right) \\ \times P_{\rm th}\left(F|\,\boldsymbol{\Theta}, \ell_i, b_i\right) P(F_i|F).\end{aligned} \tag{4b}$$

Here $P(L|\boldsymbol{\Theta})$ and $P(\ell, b, D|\boldsymbol{\Theta})$ are the luminosity function and spatial distribution, which are discussed in detail in Sections 2.1.1 and 2.1.2, respectively. The total number of sources equals the sum of the disc (N) and bulge sources ($N_{\rm bulge}$), $N_{\rm tot} = N + N_{\rm bulge}$. $P_{\rm th}(F|\boldsymbol{\Theta}, \ell, b)$ is the detection sensitivity which is defined in equation (10). We take the observed spatial positions to correspond to the true positions, since their uncertainties are negligible for the purpose of our analysis. On the other hand, we integrate over the true distances (D) and fluxes (F) of the sources. In Section 2.1.4, we discuss $P(F_i|F)$, the probability of measuring a flux (F_i), given the true flux of the source (F). Similarly, $P(\kappa_i|D)$ is the probability of observing a particular parallax or DM value (κ_i) given a true distance to the source. It is discussed separately in Section 2.2. Equations (4a) and (4b) applies to sources with (without) distance information.

In order to compute the expected number of observed sources μ we must integrate over distance, flux, and spatial coordinates. The spatial integral is performed by calculating expectations on a HEALPIX grid with NSIDE = 32 (Gorski et al. 2005). Our choice of NSIDE is driven by computational constraints. In principle, higher NSIDE yields a more accurate computation of $\mu(\boldsymbol{\Theta})$ in equation (3). For distributions with large spatial gradients higher NSIDE might be required. For disc profiles (see Section 2.1.2) such gradients are only encountered in the Galactic plane. Similarly, for bulge-like profiles spatial gradients are large near the Galactic centre. We checked explicitly that our numerical routine returns $N_{\rm tot}$ when NSIDE = 32 for the computations of equation (3) for $P_{\rm th} = 1$. Moreover, at locations with high-spatial gradients the detection sensitivity is also compromized. The weaker detection sensitivity drives the expected number of detected sources at that particular sky location to zero, neutralizing any mismodelling due to small NSIDE. For NSIDE = 32 the number of pixels is $N_{\rm pix} = 12\,288$ and $\Omega_i = 1 \times 10^{-3}$ sr. The integral is then straightforwardly performed by summing over all pixels. Since we integrate over solid angle rather than ℓ, b we divide out a factor of $\cos b$ in equation (3) which appears in $P(\ell, b, D)$. Henceforth, we drop the dependence on $\boldsymbol{\Theta}$ for notational purposes but note that the free parameters are clearly stated in Table 1.

2.1.1 Luminosity function

We test four parametrizations of the luminosity function in the range 0.1−100 GeV, namely a single power law with a hard cut-off (PL, equation 5a), single power law with superexponential cut-off (PL exp. cut-off, equation 5b), broken power law (BPL, equation 5c) and lognormal distribution (LN, equation 5d).

$$\frac{\mathrm{d}N}{\mathrm{d}L} \propto L^{-\alpha} \qquad L \leq L_{\max} \tag{5a}$$

$$\frac{\mathrm{d}N}{\mathrm{d}L} \propto L^{-\alpha} \mathrm{e}^{-(L/L_c)^{-\beta}} \tag{5b}$$

Table 1. All parameters of the likelihood with their prior values or the value they are fixed too. $L_{\max}$ is only left free in case a single power law with hard cut-off is fitted for.

Parameter	Prior	Fixed
$\log_{10}N$	[0, 8]	–
$\log_{10}N_{\rm bulge}$	[0, 8]	–
	Luminosity function	
$\log_{10}L_{\min}$	–	30
$\log_{10}L_{\max}$	[33.7, 37]	37
$\log_{10}L_c$	[32, 37]	–
$\log_{10}L_b$	[31, 37]	–
$\log_{10}L_0$	[31, 37]	–
$\alpha, \alpha_1, \alpha_2$	[0.1, 5.0]	–
σ_L	[0.5, 5]	–
β	[0, 3]	–
	Spatial profile	
B	[0, 10]	–
C	[0.05, 15]	–
z_s	[0.05, 3]	–
σ_r	[0.05, 15]	–
r_c	–	3
Γ	–	2.5
	Detection sensitivity	
$\sigma_{\rm th}$	[0.05, 3]	–
$K_{\rm th}$	[−3, 3]	–

$$\frac{\mathrm{d}N}{\mathrm{d}L} \propto \begin{cases} L^{-\alpha_1} & L \le L_b \\ L^{-\alpha_2} & L_b < L \end{cases} \tag{5c}$$

$$\frac{\mathrm{d}N}{\mathrm{d}L} \propto \frac{1}{L} \exp\left[-\frac{(\log_{10} L - \log_{10} L_0)^2}{2\sigma_L^2}\right] \tag{5d}$$

Unless specified, we fix the minimum and maximum luminosities to $L_{\min} = 10^{30}$ erg s^{-1} and $L_{\max} = 10^{37}$ erg s^{-1}, respectively. Since the luminosities of the detected pulsars are about two orders-of-magnitude away from these bounds, the derived parameters in this study are not affected by our choice of $L_{\min}$ and $L_{\max}$. The exception is the total number of sources for the single power law. However, we verified that this scales as $N_{\rm tot} \propto L_{\min}^{-\alpha+1}$, as expected when all other parameters remain unchanged. The number of free parameters varies for different scans. For a single power law we have the slope (α) and the hard cut-off ($L_{\max}$). The power law with super-exponential cut-off has the slope (α), cut-off luminosity (L_c) and β. For a broken power law we have the low- and high-luminosity slope along with the break luminosity, denoted α_1, α_2, and L_b, respectively. Finally, for the lognormal distribution we have the peak of the distribution and its width denoted L_0 and σ_L, respectively. All parameters and their prior ranges are given Table 1. The probability distributions for the luminosities are directly proportional to the luminosity function $P(L) \propto \mathrm{d}N/\mathrm{d}L$, with $\int_{L_{\min}}^{L_{\max}} P(L)\mathrm{d}L = 1$.

2.1.2 Spatial profiles

We consider two different functional forms for the disc. Each density profile is defined in cylindrical coordinates (r, z, θ) centred on the Galactic centre. The probability of finding a source at a given location is proportional to the density profile $P(r, z, \theta) = r\, n(r, z, \theta)/N$. Using the appropriate coordinate transformation (see Appendix B) this probability can be transformed to the probability of finding a source at galactic longitude and latitude (ℓ, b) and at distance D from the Sun: $P(\ell, b, D) = D^2 \cos(b) n(r, z, \theta)/N$.

Below we discuss the two parametrizations of the disc profile considered in this work, our benchmark is the Lorimer profile (Lorimer et al. 2006). In addition, we also test a model with a Gaussian radial profile (Faucher-Giguere & Loeb 2010).

Lorimer-disc profile. The Lorimer profile has a radial distribution that is described by a gamma function, whereas the z distribution follows an exponential. The number density of sources is given by Lorimer et al. (2006)

$$n(r, z) = N \frac{C^{B+2}}{4\pi R_\odot^2 z_s \mathrm{e}^C \Gamma(B+2)} \times \left(\frac{r}{R_\odot}\right)^B \times \exp\left[-C\left(\frac{r - R_\odot}{R_\odot}\right)\right] \times \exp\left(-\frac{|z|}{z_s}\right). \tag{6}$$

Here N is the number of disc sources, Γ the gamma function, B and C are parameters that define the spatial radial profile, z_s is scale height and $R_\odot = 8.5$ kpc the Solar distance from the Galactic centre. The spatial parameters B, C, and z_s are left free in the scan (see Table 1). We note that the Lorimer disc reduces to a spatial profile with an exponential radial profile as considered by Story, Gonthier & Harding (2007) for $B = 0$.

Gaussian radial profile. We also consider a spatial profile with an exponential disc and a Gaussian radial profile (Faucher-Giguere & Loeb 2010)

$$n(r, z) = N \frac{1}{4\pi \sigma_r^2 z_s} \mathrm{e}^{-r^2/2\sigma_r^2} \mathrm{e}^{-|z|/z_s}. \tag{7}$$

Bulge profile. Motivated by the GCE, we allow for the presence of a bulge population of MSPs in addition to the disc population in a subset of our scans. We model the bulge as a radial power law with a hard cut-off at $r_c = 3$ kpc and fixed slope of $\Gamma = 2.5$ (Calore et al. 2015; Daylan et al. 2016),

$$n(r) = N_{\rm bulge} \frac{3 - \Gamma}{4\pi r_c^{3-\Gamma}} r^{-\Gamma}. \tag{8}$$

Again, $P(\ell, b, D) = D^2 \cos(b) n(r, \theta, \phi)/N_{\rm bulge}$ (see Appendix B).

Recently, it was found that the GCE is better described by a morphology that traces the triaxial boxy bulge instead of a spherically symmetric profile (Bartels et al. 2018; Macias et al. 2018). Nevertheless, we model the bulge MSP population with a radial power law. The goal is to test whether this component is required by the data at all. We do not expect this analysis to be sensitive to the exact morphology of the bulge.

2.1.3 Detection sensitivity

We allow for some uncertainty in the Fermi detection sensitivity. Depending on the data set we use, the true detection efficiency can be an arbitrarily complicated function. In particular for confirmed pulsars, many of which have been detected by folding in the radio pulsation period, it does not only depend on the γ-ray brightness of a source, but also on the radio properties of the pulsar population and the sensitivity of current radio telescopes. Therefore, we expect the sensitivity to be different from the Fermi detection sensitivity. Here we follow the same procedure as (Hooper & Mohlabeng 2016;

Ploeg et al. 2017) to model the detection sensitivity. The threshold flux at a given sky position is drawn from a lognormal distribution

$$P(F_{\rm th}|\ell, b) = \frac{1}{\sigma_{\rm th} F_{\rm th}\sqrt{2\pi}} \times \exp\left[-\frac{\left(\ln F_{\rm th} - \left(\ln(F_{\rm th,\,mod.}(\ell, b)) + K_{\rm th}\right)\right)^2}{2\sigma_{\rm th}^2}\right], \tag{9}$$

where $3.2F_{\rm th,\,mod.}(\ell, b)$ corresponds to the sensitivity map in fig. 16 of Abdo et al. (2013). We have two free parameters $K_{\rm th}$ and $\sigma_{\rm th}$, respectively, the normalization and width of the distribution from which $F_{\rm th}$ is drawn. A source is detected if $F \geq F_{\rm th}$, therefore

$$P_{\rm th}(F|\ell, b) \equiv P(F \geq F_{\rm th}|\ell, b) = \frac{1}{2} + \frac{1}{2}{\rm erf}\left[\frac{\ln F - \left(\ln(F_{\rm th,\,mod.}(\ell, b)) + K_{\rm th}\right)}{\sqrt{2}\sigma_{\rm th}}\right]. \tag{10}$$

2.1.4 *Flux uncertainties*

Energy fluxes (0.1−100 GeV) and their uncertainties are taken from the 2FGL (Nolan et al. 2012), 3FGL (Acero et al. 2015), or the preliminary Fermi–Lat 8 yr catalogue (FL8Y).[1] The flux uncertainties are treated as Gaussian, the probability of observing a flux ($F_{\rm obs}$) given some true flux (F) is

$$P(F|F_{\rm obs}) = \frac{1}{\sqrt{2\pi\sigma_F^2}} {\rm e}^{-(F-F_{\rm obs})^2/2\sigma_F^2}, \tag{11}$$

where $F_{\rm obs}$ and σ_F are the observed energy flux (≥0.1 GeV) and its associated uncertainty.

2.2 Distances

There are two primary methods for measuring the distances to pulsars. If they are close enough to our galactic position it can be possible to obtain a parallax distance measure, typically accepted as the most unbiased method to measure distances to pulsars. However, for the majority of pulsars the only distance measure comes from radio observations of the DM, a frequency dependent time shift of the pulse profile. In order to take into account uncertainties in the distance estimates we construct a realistic probability-density function (PDF) for the probability of measuring a specific parallax ($w_{\rm obs}$) or DM$_{\rm obs}$ given a true distance to the source: $P(\kappa_{\rm obs}|D)$ with $\kappa_{\rm obs}$ being the parallax or DM. In the likelihood we then integrate over D. If parallax information is available we construct distance PDFs using these measurements, otherwise we use DM information. In case neither is available, this term is not present in the likelihood (equation 4b).

2.2.1 *Distance from parallax*

For a small number of MSPs in our sample parallax information is available (see Table A1). True parallaxes ($\omega(D) \equiv 1/D$) and measured uncertainties ($\sigma_{\omega_\pm}$) are used to construct a PDF for the observed parallax $\omega_{\rm obs}$. The error on the parallax is taken to be Gaussian, but can be asymmetric. The PDF for the distance can then be constructed as follows (Verbiest et al. 2012)

$$P\left(\omega_{\rm obs}|\omega(D)\right) \propto \Theta_H\left(\frac{1}{D} - \omega_{\rm obs}\right)\exp\left[-\frac{1}{2}\left(\frac{\omega_{\rm obs} - 1/D}{\sigma_{\omega_+}}\right)^2\right] + \Theta_H\left(\omega_{\rm obs} - \frac{1}{D}\right)\exp\left[-\frac{1}{2}\left(\frac{\omega_{\rm obs} - 1/D}{\sigma_{\omega_-}}\right)^2\right], \tag{12}$$

where Θ_H is the heaviside-step function.

2.2.2 *Distance from DM*

The origin of the DM is assumed to come from interactions with free electrons along the line of sight. Assuming a particular distribution of free electrons in the Galaxy we can therefore calculate the distance to any given pulsar using,

$$\mathrm{DM} = \int_0^D n_{\rm e}(l)\,{\rm d}l\,, \tag{13}$$

where $n_{\rm e}$ is number density of electrons along the line of sight. Whereas the DM for each source is well constrained, $n_{\rm e}(l)$ is a source of large uncertainties for individual sources (Lorimer 2001) and sometimes the cause of systematic biases (Yao et al. 2017). To date there are three main models for $n_{\rm e}$: TC93 (Taylor & Cordes 1993), NE2001 (Cordes & Lazio 2002; used by the majority of past MSP luminosity function analyses), and the recent YMW16 (Yao et al. 2017). Yao et al. (2017) showed that the YMW16 model was less affected by the large errors which typically entered the NE2001 model, particularly at high galactic latitudes, the regime in which NE2001 was shown to have large systematic biases (Roberts 2011). We assume the YMW16 model as a description of the electron density. The YMW16 model contains 35 free parameters describing a variety of galactic components contributing to the total electron density, for e.g. the scale height of the thick disc. In principle these could all affect the distance calculated to a given source. For each pulsar a PDF is generated for the observed DM as a function of true distance. We adopt a conservative approach by sampling from all variable parameters and calculating the DM for each pulsar given a true distance to the source. Gaussian distributions around each parameter are assumed with the central values and 1 σ errors as provided in table 2 of Yao et al. (2017). We sample 10^5 combinations of parameters and true distances for each pulsar and create a PDF by binning the data in a histogram. An example is provided in Fig. 1. Using this method, we found that the PDF always peaks extremely close to the best-fitting value from the YMW16 model but there can be quite significant spread, even though most of the parameters in the YMW16 model are quite well constrained.

All code to reproduce the DM-based PDFs for either the DM or the distance to an individual pulsar is publicly available at https://github.com/tedwards2412/MSPDist. We provide a PYTHON wrapper for the YMW16 electron-density model (Yao et al. 2017) and accompanying code to calculate distance uncertainties.

2.3 Pulsar sample

2.3.1 *γ-ray detected pulsars*

In our benchmark analysis we exclusively use the γ-ray detected MSPs not associated with a globular cluster. All sources have spin periods ≤30 ms. Our sample contains 96 sources with confirmed γ-ray pulsations (see Table A1). The source list is compiled using the second pulsar catalogue (2PC) (Abdo et al. 2013) and the public list of *Fermi*–LAT detected γ-ray pulsars as was available on 2018

[1] https://fermi.gsfc.nasa.gov/ssc/data/access/lat/fl8y/

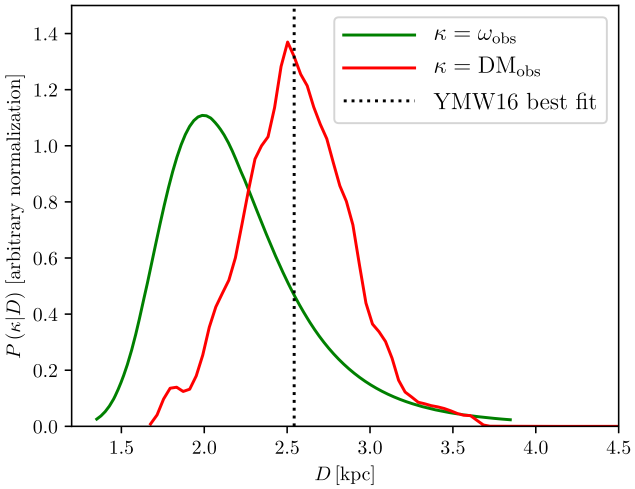

Figure 1. Probability distribution for the measured parallax and DM of J1600−3053 given the true distance of the source. PDFs have an arbitrary normalization. The black-dotted line shows the distance corresponding the observed DM and the best-fitting parameters of the YMW model. Varying the parameters of the YMW16 model yields the distribution shown in red. The green line corresponds to the PDF for the parallax.

May 14.[2] Unless specified otherwise, fluxes are taken from the third *Fermi*–LAT source catalogue (3FGL; Acero et al. 2015). When a pulsar is not present in the 3FGL we also look for fluxes in the second *Fermi*–LAT source catalogue (2FGL; Nolan et al. 2012), and the FL8Y. Similarly, parallax and DMs are obtained from the ATNF catalogue (Manchester et al. 2005).

2.3.2 *Unassociated sources*

The 3FGL contains 3033 objects with roughly a third still unassociated to a particular source type. Follow-up radio observations of many of the unassociated sources have shown that there could be a large population of pulsars still remaining to be found within the 3FGL. If only a small proportion turn out to be MSPs this population will still tend to dominate the overall data set. We therefore must attempt to take this population into account and see how it could systematically affect our results. We capture the possible effects of the unassociated sources by presenting three scenarios. First, we perform our analysis using only the 96 γ-ray detected sources. In addition, we perform the same analysis using only the 39 MSPs present in the 2PC. Finally, we combine the 96 γ-ray detected sources with 69 sources without γ-ray detected pulsations based on the results from Saz Parkinson et al. (2016). Although some of these 69 sources have unconfirmed associations, we will refer to this sample as unassociated sources for conciseness. These can be found in Table A1 under 'other sources'.

Saz Parkinson et al. (2016) performed a classification analysis of the 3FGL using a variety of Machine Learning tools, the most accurate being Random Forest which achieved >90 per cent correct associations when trained on 70 per cent of the sample and tested on the remaining 30 per cent. For the construction of our unassociated sample, we select all 3FGL unassociated sources and source candidates of any given class that have not been confirmed. We require that each source is classified as a pulsar by either the logistic regression or Random Forest analysis of Saz Parkinson et al. (2016) with over 50 per cent probability. Moreover, we require the same classifier to classify the candidate as an MSP rather than a young pulsar. Finally, we require a detection significance in the 3FGL or FL8Y of $\geq 10\,\sigma$, similar to the list in table 6 of Saz Parkinson et al. (2016) to optimize the chances of the classification being correct. We note a few of the prime candidates in this table have since been discovered as γ-ray MSPs, including the two recent detections by Clark et al. (2018).

[2] https://confluence.slac.stanford.edu/display/GLAMCOG/ Public+List+of+LAT-Detected+Gamma-Ray+Pulsars

2.4 Parameter scan

We efficiently scan the parameter space using the Bayesian nested sampling package `MultiNest` (Feroz, Hobson & Bridges 2009; Buchner et al. 2014). For the low-dimensional problems at hand, `MultiNest` is accurate and requires a computationally feasible number of likelihood calculations to accurately map the posterior distribution. In addition it is able to handle multimodal distributions and degeneracies in the parameter space, the latter being a problem we are likely to encounter when considering particular configurations of luminosity functions, such as PL with a maximum luminosity cut-off. The results presented in Section 3 use `nlive` = 500.

For each model the Bayesian evidence is computed (e.g. Trotta 2008)

$$\mathcal{Z} = P(\mathcal{D}) = \int \mathcal{L}(\mathbf{\Theta})\pi(\mathbf{\Theta})d\mathbf{\Theta}, \tag{14}$$

where $\pi(\Theta)$ is the prior on each parameter. The Bayes factor is then defined as

$$B_{12} \equiv \frac{P\left(H_2|\,\mathcal{D}\right)}{P\left(H_1|\,\mathcal{D}\right)} = \frac{\mathcal{Z}_2\,P(H_2)}{\mathcal{Z}_1\,P(H_1)}, \tag{15}$$

with $H_{1,\,2}$ denoting the different models (Trotta 2008). We choose equal priors for different models, $P(H_2)/P(H_1) = 1$. Since our models are not nested hypotheses, Bayesian model selection, which does not require this assumption, provides a straightforward comparison of our models. We note that, in contrast to Frequentist analyses, it is here relevant to properly normalize the likelihood functions in order to make the evidence and the Bayes factor informative. The expressions in equations (1) and (4) ensure this.

3 RESULTS

3.1 Model comparison

For each of the three data sets[γ-ray detected MSPs, MSPs plus MSP candidates from Saz Parkinson et al. (2016) and the 2PC MSPs] we compare multiple models, each characterized by their luminosity function, spatial profile and whether or not we included a bulge population.

In order to interpret the results we use Bayesian model comparison following Kass & Raftery (1995). We compute $2\ln B_{12}$ from equation (15) always comparing against a benchmark model (H_2: BPL, Lorimer). If $2\ln B_{12} \in [0, 2]$ there is no preference for H_2 over H_1. $2\ln B_{12} > 10$ represents strong preference for H_2. Contrarily, $2\ln B_{12} < 0$ indicates H_1 is preferred over H_2.

The results for the various `MultiNest` scans performed are shown in Table 2. Each data set is shown separately and models are ordered by decreasing $\mathcal{Z}$. Our default data set (γ-ray detected pulsars only) shows that a single power-law parametrization of the luminosity function, regardless of whether it has a hard or super-exponential cut-off, is greatly disfavoured. No strong preference is

Table 2. Model comparison for the three different data-sets analysed. Each model is characterized by the luminosity function, spatial profile and whether or not we included a bulge population. We show the log of the Bayesian evidence ($\ln \mathcal{Z}$) for each model and the Bayes factor ($B_{12} = 2\ln \mathcal{Z}_2/\mathcal{Z}_1$) with respect to the best-fitting model without bulge (Kass & Raftery 1995).

Model	$\ln \mathcal{Z}$	$2\ln B_{12}$
	γ-ray detected pulsars	
BPL, Lorimer	2042.0	0.0
BPL, Lorimer, bulge	2041.6	0.8
LN, Lorimer	2040.0	4.0
LN, Lorimer, bulge	2040.0	4.0
PL exp. cut-off, Lorimer	2036.6	10.8
BPL, Gaussian	2024.0	36.0
BPL, Gaussian, bulge	2023.7	36.6
LN, Gaussian	2021.8	40.4
LN, Gaussian, bulge	2021.2	41.6
PL, Lorimer	2017.6	48.8
	All sources	
BPL, Lorimer	3889.6	0.0
BPL, Lorimer, bulge	3889.6	0.0
LN, Lorimer, bulge	3888.9	1.4
LN, Lorimer	3888.3	2.6
BPL, Gaussian	3875.9	27.4
LN, Gaussian	3874.4	30.4
	2PC	
BPL, Lorimer	789.0	0.0
LN, Lorimer	787.9	2.2
BPL, Gaussian	780.0	18.0
LN, Gaussian	778.8	20.4

present for either a lognormal or broken power-law parametrization, although the latter performs slightly better. Concerning the spatial profile, the Lorimer disc is strongly preferred over the radial Gaussian profile. No bulge component is required by the data. A small point of caution, in a few cases the evidence of models including the bulge is smaller than of identical models without a bulge component. However, the likelihood for the models including the bulge is higher than that of those where it is not included, which is expected when including additional degrees of freedom. The fact that the evidence goes down with the addition of a new component means that the model without the additional component suffices to describe the data. Given these results, we will henceforth consider the Lorimer disc with a BPL luminosity function and no bulge as our benchmark model and show results for this run. Additional results can be found in Appendix D.

3.2 Parameters

In Fig. 2 we show a corner plot for the parameters of our benchmark model. Contours in the two-dimensional histograms are 1, 2, and 3σ. Dashed-lines in the one-dimensional posterior represent 16, 50, and 84 per cent quantiles. The best-fitting parameters for our benchmark model and for the lognormal luminosity function with a Lorimer disc are given in Table 3. Corner plots for other representative models in Table 2 are presented in Appendix D.

The total number of sources with $L \geq L_{\min}$ is $\sim 2 \times 10^4$ for our best-fitting model. However, it could be as small as $\sim 10^4$ or as large as $\sim 10^5$. Unlike previous claims (Grégoire & Knödlseder 2013), we find the γ-ray MSP population to be compatible with the expected number of MSPs from population studies using radio pulsars (Cordes & Chernoff 1997; Lyne et al. 1998; Levin et al. 2013).

Luminosity function. In Fig. 3 we show the luminosity function. The blue solid line displays the total luminosity function, whereas the dashed line shows the luminosity function with the detection efficiency folded in. The grey-shaded area corresponds to one or fewer sources at this luminosity.

Orange errorbars show the expectation values derived from the data. Uncertainties in the flux and distance to individual pulsars have been taken into account (see Appendix C2). Upper limits correspond to an expectation of fewer than one source in the particular bin. In addition, we show the cumulative distribution of the luminosity function in Fig. 4. The data point and errorbars show the median and the 95 per cent containment interval.

At $\sim 2 \times 10^{33}$ erg s^{-1} there is a clear turnover. Due to the hard slope at low luminosities ($\alpha_1 = 1.0$) and soft slope at high luminosities ($\alpha_2 = 2.6$) the total flux is dominated by sources somewhat below the break luminosity. There is no indication of any MSPs brighter than few $\times\, 10^{35}$ erg s^{-1} or dimmer than $\sim 10^{32}$ erg s^{-1}. This parametrization broadly agrees with the results from Winter et al. (2016).

Spatial profile. Spatial parameters are not very well constrained. The scale height of the disc is $\sim$0.7 kpc but has an uncertainty of a factor $\sim$1.5, in broad agreement with earlier works (e.g. Story et al. 2007; Levin et al. 2013; Calore, Di Mauro & Donato 2014; Hooper & Mohlabeng 2016; Ploeg et al. 2017). The radial parameters of the Lorimer profile are consistent with the distribution derived for the full radio pulsar population (Lorimer 2003; Lorimer et al. 2006) and with expectations for the MSP population (Lorimer et al. 2015). For the Gaussian profile (see Appendix D), the dispersion is $\sigma_r \sim 4$ kpc, but is again uncertain by $\sim$25 per cent. This result is consistent with the expectations for an old pulsar population Faucher-Giguere & Loeb (2010). Our results for the spatial profile are also in agreement with other analyses of γ-ray MSPs (Hooper & Mohlabeng 2016; Ploeg et al. 2017).

In Figs 5 and 6 we show the expected (blue) and observed (orange) latitude and longitude distribution of γ-ray detected MSPs.

Detection sensitivity. In principle, the parameters $\{K_{\rm th}, \sigma_{\rm th}\}$ are nuisance parameters. For the different data sets, i.e. 2PC, γ-ray detected pulsars, and including not-yet-identified sources, we find $\{K_{\rm th}, \sigma_{\rm th}\} = \{2.05, 0.64\}, \{1.35, 0.41\}$, and $\{1.19, 0.30\}$, respectively. The detection sensitivity improves with a larger sample size as expected since a larger sample implies either increased exposure, such as when going from the 2PC to the benchmark full γ-ray detected pulsars sample, or more lenient detection criteria, such as when we include unassociated sources. Recall that there is a rescaling of our sensitivity map with respect to fig. 16 of Abdo et al. (2013) of a factor 3.2 (see Section 2.1.3). The rescaling obtained from our fit corresponds to $\exp(K_{\rm th})$. The values obtained for $K_{\rm th}$ in our benchmark model thus indicate a sensitivity that is slightly worse by a factor $\sim$1.2 compared to fig. 16 of Abdo et al. (2013), despite a larger exposure. However, this is not unreasonable given that Abdo et al. (2013) derived their map assuming γ-ray sources with a pulsar-like spectrum, but did not require pulsations to be detected. In Fig. 7 we show the energy flux of the 96 γ-ray detected MSPs in our sample compared to the 10 per cent–90 per cent percentile of the best-fitting flux sensitivity as a function of latitude. The figure

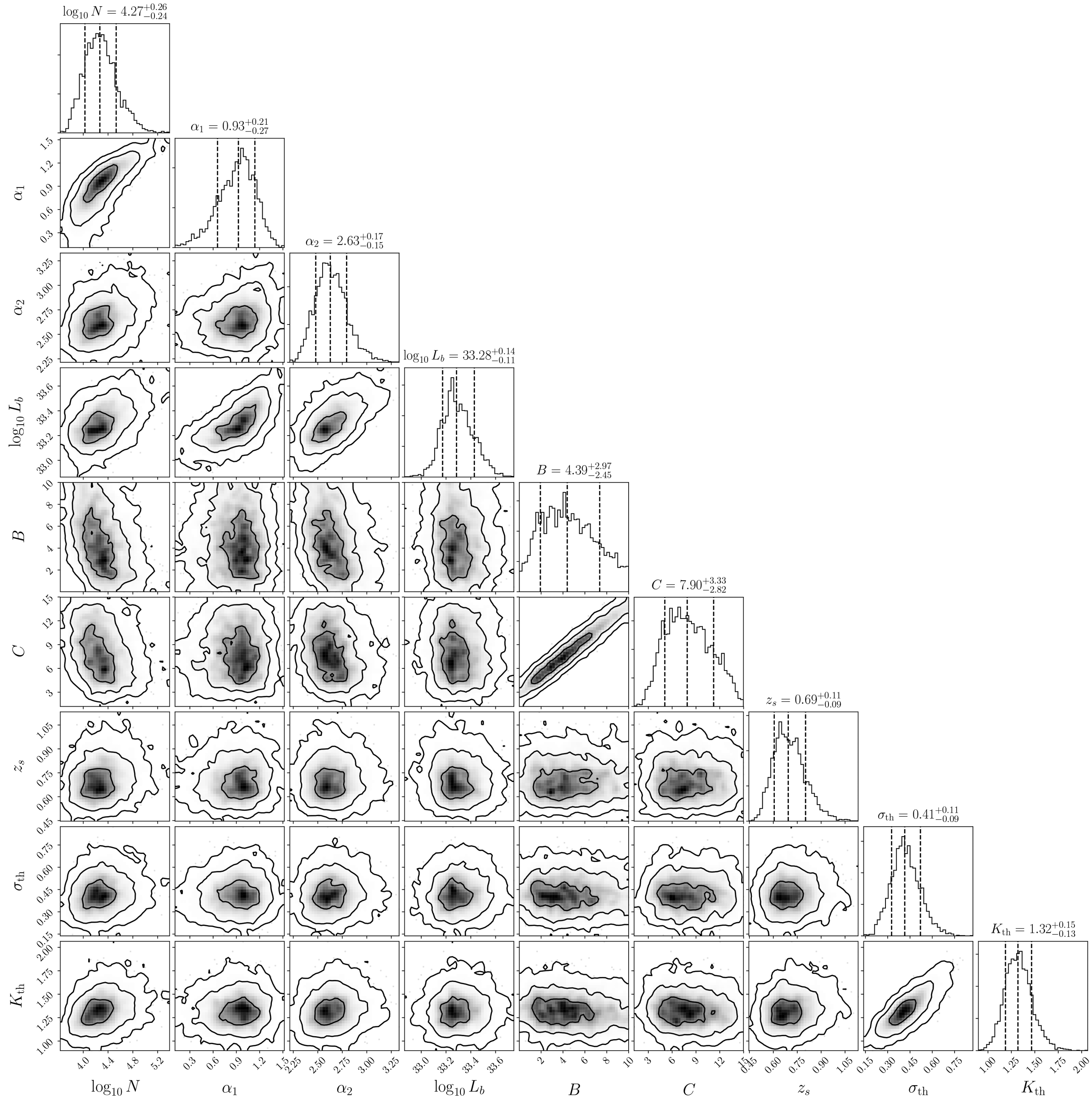

Figure 2. Corner plot for the parameters of our benchmark model. Contours in the two-dimensional histogram are 1, 2, and 3 σ. Dashed-lines in the one-dimensional posterior show the 16, 50, and 84 per cent quantiles. Values above each posterior represent the 50 per cent quantile with 1 σ errors.

is similar to fig. 17 of Abdo et al. (2013). MSPs are detected upto the flux threshold, as expected.

For completeness, we show the flux distribution in Fig. 8. The blue solid line is the total population, whereas the blue dashed line takes into account the detection threshold. As can be seen our analysis suggests the MSP population is flux complete down to $F \gtrsim 10^{-11}\,\mathrm{erg\,cm^{-2}\,s^{-2}}$.

3.3 TOTAL LUMINOSITY AND FLUX

Given the number of sources and luminosity function we can determine the total luminosity. Since the broken power law peaks at luminosities of $\sim 10^{33}\,\mathrm{erg\,s^{-1}}$ and has a hard (soft) slope at low (high) luminosities, the total luminosity is fairly insensitive to $L_{\rm min}$ and $L_{\rm max}$. The same holds for the lognormal distribution. We find a total luminosity $L_{\rm tot} = 1.5 \times 10^{37}\,\mathrm{erg\,s^{-1}}$ and a total flux of $4.7 \times 10^{-9}\,\mathrm{erg\,cm^{-2}\,s^{-1}}$. These numbers are uncertain by about a factor $\sim$2. Given a Milky Way stellar-disc mass of $5.17 \times 10^{10}\,\mathrm{M_\odot}$ (Licquia & Newman 2015) we find that luminosity-per-stellar-mass for the Milky Way disc is $2.9 \times 10^{26}\,\mathrm{erg\,s^{-1}\,M_\odot^{-1}}$.

Table 3. Best-fitting parameters and characteristics for the populations with a broken power law and lognormal luminosity function and Lorimer-disc spatial profile. Luminosities and fluxes are in the range 0.1–100 GeV.

Parameter	Broken power law	Lognormal
	Luminosity function	
$\log_{10}L_{\min}$	30	30
$\log_{10}L_{\max}$	37	37
α_1	0.97	–
α_2	2.60	–
$\log_{10}L_b$	33.24	–
$\log_{10}L_0$	–	32.61
σ_L	–	0.63
	Spatial profile	
B	3.91	2.75
C	7.54	5.94
z_s	0.76	0.63
	Detection sensitivity	
$\sigma_{\rm th}$	0.41	0.45
$K_{\rm th}$	1.35	1.33
	Other characteristics	
$\log_{10}N$	4.38	4.12
$\langle L\rangle$ [erg s^{-1}]	6.2×10^{32}	1.1×10^{33}
$L_{\rm tot}$ [erg s^{-1}]	1.5×10^{37}	1.5×10^{37}
$F_{\rm tot}$ [erg cm^{-2} s^{-1}]	4.7×10^{-9}	4.8×10^{-9}
Expected bulge detections	4.5	2.9

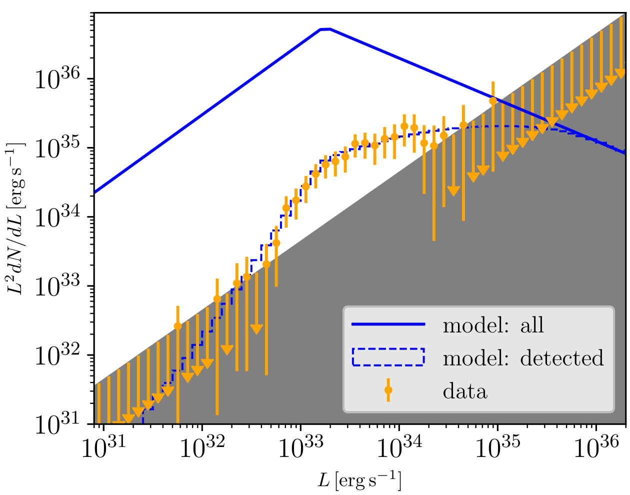

Figure 3. Luminosity function (0.1–100 GeV) of our benchmark model. The blue solid line shows the total luminosity function, whereas the dashed line only shows the expected sources. Orange errorbars are the expectations-values from the data where distance and flux uncertainties have been taken into account (for more details see Appendix C2). The grey-shaded area corresponds to one or fewer sources.

4 DISCUSSION

4.1 Unassociated sources

Our default analysis includes 96 γ-ray detected MSPs. In addition, we performed analyses using only the 39 MSPs from the 2PC (Abdo et al. 2013) and including an additional 69 unassociated sources with selection criteria based on the results of Saz Parkinson et al. (2016).

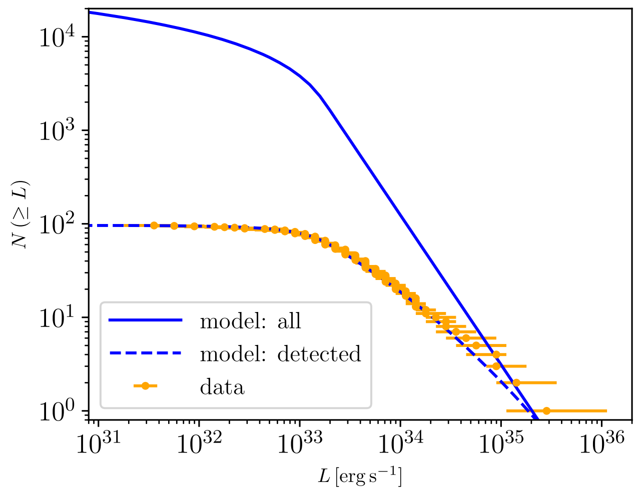

Figure 4. Similar to Fig. 3, but showing the cumulative distribution. Distance and flux uncertainties for individual pulsars are included in the errorbars, which show the median and 95 per cent containment interval.

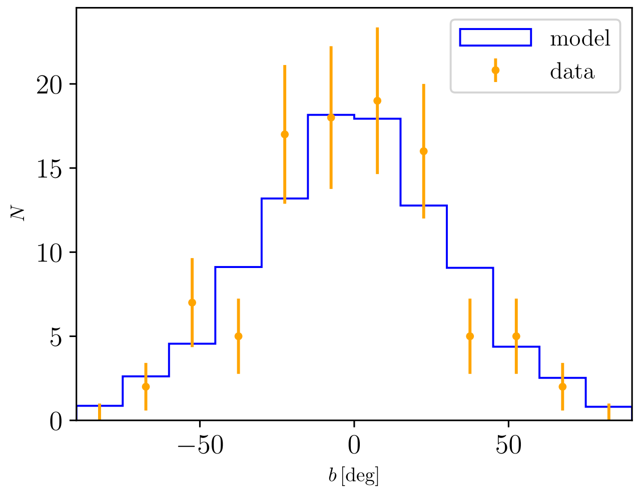

Figure 5. Latitude distribution of MSPs. Blue is the expected distribution. Orange data points show the observed distribution.

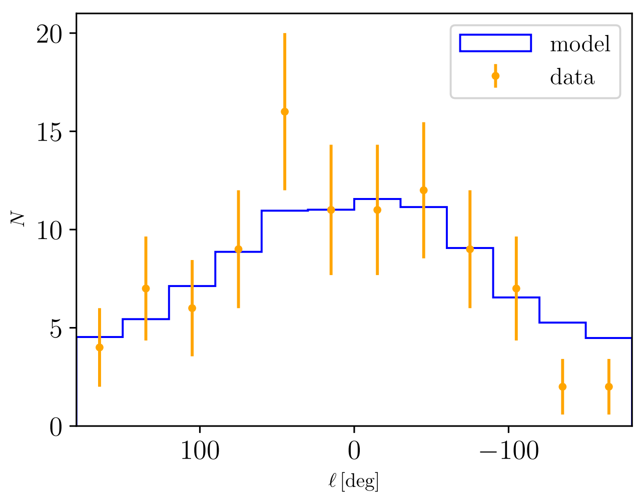

Figure 6. Same as Fig. 5 but for longitude.

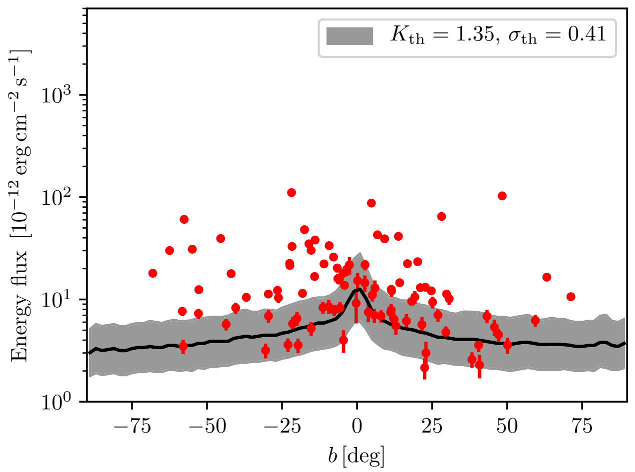

Figure 7. 0.1–100 GeV energy flux and latitude of the 96 γ-ray detected MSPs compared to the 10 per cent–90 per cent percentile flux sensitivity at each latitude. The figure is similar to fig. 17 in Abdo et al. (2013).

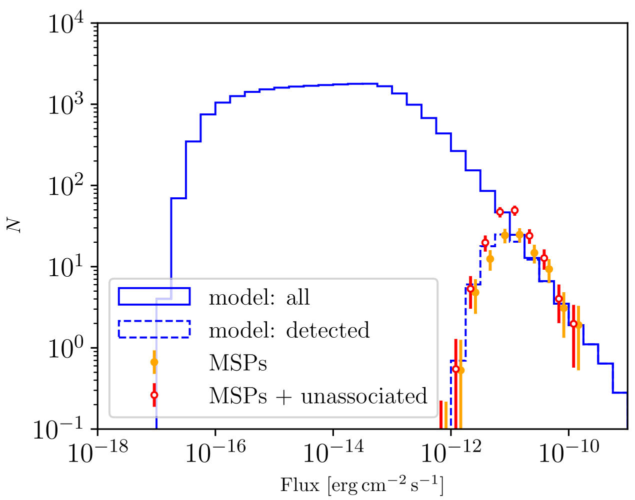

Figure 8. Flux distribution for our benchmark model. The blue solid line is the total MSP population. The dashed blue line takes into account the detection threshold. Orange errorbars are the data including all γ-ray detected pulsars. Red-open errorbars also include the 69 unassociated sources. Note that the blue-dashed line corresponds to the detection sensitivity derived using only the γ-ray detected pulsars.

We find consistent results between the three analyses. In particular, as can be seen in Table 2, in all cases we find that there is no clear preference for either a broken power law or a lognormal luminosity-function parametrization. On the other hand, the Lorimer profile is always preferred over the Gaussian disc. Moreover, the inferred parameters agree within errors between different data sets, but get more tightly constrained by larger data sets (see Figs 2, D4 and D5).

This leads us to the somewhat surprizing conclusion that for the purpose of our analysis there is no strong bias when including only γ-ray detected MSPs in the analysis. A priori this is not obvious, since all but one source have radio counterparts which could lead to a selection bias which cannot be efficiently accounted for in the detection sensitivity. Moreover, for all but one of the unassociated sources we do not have distance priors. This analysis however shows that we can derive consistent constraints whether or not distance information is included (also see Hooper & Mohlabeng 2016).

In the future, it would be interesting to include a larger sample of likely pulsar candidates in order to constrain the luminosity function down to lower fluxes. In particular, without radio counterpart, it is difficult to confirm γ-ray pulsations in blind searches (Clark et al. 2018). One possibility would be an update of the work by Saz Parkinson et al. (2016) using a larger source catalogue. In addition, Ajello et al. (2017)[3] propose a potentially powerful technique which classifies unassociated sources as likely pulsar candidates and which uses a customized detection efficiency.

4.2 Implications for the Galactic centre excess

We tested for the presence of a bulge MSP population by including an additional component in our analysis (Section 2), but find no evidence for the presence of such a population (Section 3). This analysis assumes that bulge MSPs follow the same luminosity function as disc MSPs. Using the same assumption and the observed GCE intensity we can also estimate how many MSPs from the bulge should have been detected. We use a GCE intensity of $2.3 \times 10^{-9}\,{\rm erg\,cm^{-2}\,s^{-1}}$ (Bartels et al. 2018) and distance to the GCE of $R_\odot = 8.5$ kpc to normalize the bulge population. Using the best-fitting detection efficiency and luminosity function of our benchmark model we estimate that 4.5 sources should have been detected. Within the 95 per cent containment interval of the full posterior the number of bulge MSP detections ranges from being fewer than one to more than a dozen. Using the data set that includes unassociated sources, this number goes up to 5.5. Similar numbers are obtained for the lognormal luminosity function. We therefore agree with Ploeg et al. (2017) that the MSP interpretation of the GCE is consistent with the luminosity function derived from MSPs in the Galactic disc.

We find that opposite conclusions are driven by the high-luminosity tail of the luminosity function. At the distance of the GC mostly sources with luminosities $\gtrsim 2 \times 10^{34}\,{\rm erg\,s^{-1}}$ can be detected. Hooper & Mohlabeng (2016) find relatively more bright sources ($\geq 10^{34}\,{\rm erg\,s^{-1}}$), and thus a higher number of expected bulge detections, compared to this work and Ploeg et al. (2017). Similarly, the MSP population in globular clusters has about an order-of-magnitude higher mean luminosity than what we derive for the disc (Hooper & Linden 2016). The treatment of the flux threshold only has a mild impact. Here and in Ploeg et al. (2017) both $K_{\rm th}$ and $\sigma_{\rm th}$ are left free in the fit. However, Hooper & Mohlabeng (2016) fix $\sigma_{\rm th} = 0.9$, which is larger than our best-fitting value. Although this leads to a larger acceptance of dim sources, the detection probabilities at $\gtrsim 3 \times 10^{34}\,{\rm erg\,s^{-1}}$ are very similar.

It should be mentioned that all but one of the γ-ray detected MSPs have radio counterparts. It is notoriously difficult to detect MSPs in radio near the Galactic centre due to the large scatter broadening of pulsed emission (e.g. Calore et al. 2016). Since we apply a detection threshold based on γ-ray flux this does not directly take into account the decreasing sensitivity of radio searches with increasing distance. Consequently, if bulge MSPs are present in our full sample it is not unlikely that they are all unassociated sources. In the near future, the radio sensitivity for searches of bulge MSPs should increase significantly, allowing for the detection of this component in radio (Calore et al. 2016).

If the GCE originates from MSPs in the disc we find a bulge-to-disc (*B/D*) luminosity (flux) ratio of $B/D \sim 1.3\,(0.5)$. The ratio of luminosity-to-stellar mass in the bulge is $2.2 \times 10^{27}\,{\rm erg\,s^{-1}\,M_\odot^{-1}}$

[3] Also see Bartels et al. (2018).

compared to 2.9×10^{26} erg s^{-1} M$_{\odot}^{-1}$ in the disc. Therefore, the bulge appears to host approximately eight times more MSPs per unit stellar mass than the disc, consistent with the results from Bartels et al. (2018).

4.3 Completeness

We discuss the completeness we obtain from our analysis, i.e. the number of detected sources over the total number of sources in the disc, and compare it to the results of Winter et al. (2016). Although Winter et al. (2016) find a comparable parametrization of the luminosity function, their normalization and therefore total luminosity is about a factor 7 larger than what we find (Winter et al. 2016; Eckner et al. 2017). This difference can be ascribed to the fact that our analysis yields a larger completeness by about a factor $\sim$10 at the peak of the luminosity function ($L \sim 10^{33}$ erg s^{-1}). It should be taken into account that we use a larger sample of MSPs, 96 versus 66 in Winter et al. (2016). Naively rescaling by this ratio still leaves a factor $\sim$7 higher completeness.

We find the reason for the difference in completeness to be two-fold. First, Winter et al. (2016) estimate completeness by performing a Monte Carlo (MC) simulation. They randomly draw pulsars at a given luminosity and assign it a position by drawing from a Lorimer profile with $B = 0$, $C = 2.8$, and $z_s = 0.6$ (Story et al. 2007; Grégoire & Knödlseder 2013; Winter et al. 2016). In fact, C and z_s are themselves also drawn from lognormal distribution. This profile is consistent with our best-fitting value at $\sim 2\,\sigma$. We compare the impact this has on the completeness by running a MC simulation drawing sources at different luminosities and assigning them spatial positions based on the distribution assumed in Winter et al. (2016) and our benchmark distribution. With the spatial profile from Winter et al. (2016) the MSPs are on average slightly further away compared to our benchmark spatial profile. Consequently, the flux received from each source is about a factor $\sim$2 dimmer, which so happens to also result in a loss of completeness by a factor $\sim$2. This is displayed Fig. 9 as the difference between the green and red lines with the same linestyle. Secondly, the detection threshold applied by Winter et al. (2016) is based on latitude dependent flux threshold in fig. 17 from Abdo et al. (2013), whereas we use the map in fig. 16 of that same work. In our MC simulation we also compare these two detection sensitivities. In Fig. 9 this is shown by the difference between the solid (our detection sensitivity) and dashed (sensitivity threshold from Winter et al. 2016) lines of the same colour. We find that our sensitivity function yields a larger completeness. Finally, we note that in our MC simulation the red solid line corresponds to our benchmark model and the green solid line to our reproduction of the completeness from Winter et al. (2016), with their spatial distribution and flux threshold. In the bottom panel we show the ratio of the red-solid line (our work) over the green-dashed line (our MC reproduction of Winter et al. 2016, which agrees very well).

A merit of our analysis is that it is fully self-consistent in that we model the spatial-distribution, luminosity function, and flux sensitivity simultaneously. Therefore, we consider the grey band in Fig. 9 to be the most trustworthy representation of the completeness. It shows the 68 per cent and 95 per cent containment interval of the completeness for our benchmark model. We construct it by sampling spatial and flux-sensitivity parameters from the full `MultiNest` posterior and consecutively running a MC simulation to estimate the completeness for each point.

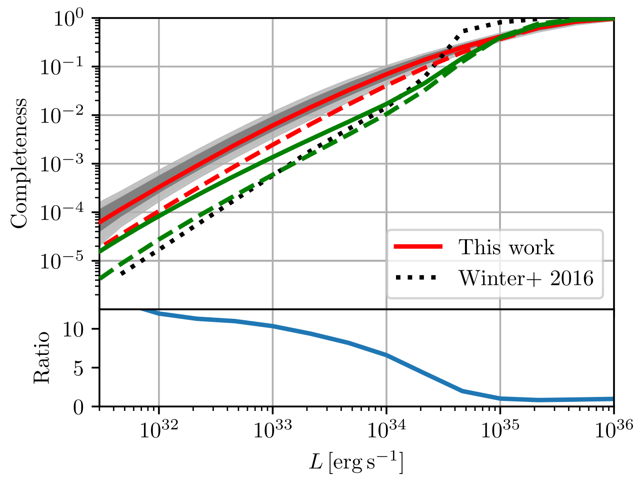

Figure 9. *Top panel:* Comparison of completeness between this work (solid-red line) and Winter et al. (2016) (black dotted line). The dark (light) grey band shows the 68 per cent (95 per cent) containment interval of the completeness obtained in this work. Colour and line style indicate spatial distribution and flux threshold, respectively. Red (green) use the spatial distribution from this work (Winter et al. 2016). The solid (dashed) lines use the flux threshold from this work (Winter et al. 2016). The green dashed line shows our reproduction of the MC simulation of Winter et al. (2016), using their spatial distribution and flux sensitivity. *Bottom panel:* ratio of the red-solid over the green-dashed line.

The estimated completeness at the peak of the luminosity function has a large impact on the derived ratio of emission per unit stellar mass and therefore the expected unresolved flux. Any conclusions that relies directly on the completeness by estimating the luminosity of MSPs in a given environment by applying the luminosity-per-stellar mass from the disc is affected by this uncertainty. With our estimate of the completeness we expect MSPs from the disc to contribute $\mathcal{O}(1$ per cent) to the total γ-ray flux from 1−10 GeV, where the MSP spectrum is most pronounced (McCann 2015). Moreover, studies of dwarf spheroidal galaxies (Winter et al. 2016), Andromeda (Eckner et al. 2017), and the Galactic Bulge (Bartels et al. 2018; Macias et al. 2018) are also affected by our estimated completeness.[4]

4.4 Remarks on the detection sensitivity

In this work we used the sensitivity map from Abdo et al. (2013) with two free parameters, the normalization ,and a parameter that allows for spread in the detection sensitivity. Abdo et al. (2013) constructed the map with the dedicated purpose of characterizing the detection sensitivity for a γ-ray source with a pulsar-like spectrum (power law with exponential cut-off). In addition it applies to 3 yr of data and does not make any assumptions about the detection of pulsed emission (for more details see section 8.2 of Abdo et al. 2013). Consequently, this map is not tailored to our study. Nevertheless, we believe that the sensitivity map as applied is a reasonable approximation and does not lead to evident biases for the reasons listed below.

Since we look at pulsars the spectrum for which the map has been constructed is compatible. Moreover, the spatial features in the map come from the γ-ray background which does not depend on the

[4]The uncertainty in the completeness and its impact were already briefly discussed in Bartels et al. (2018) and Eckner et al. (2017).

type of source. Finally, with increasing observation time ($t_{\rm obs}$) the sensitivity should improve as $1/\sqrt{t_{\rm obs}}$, which can be captured by our rescaling factor $K_{\rm th}$.

We checked explicitly that our results do not critically depend on the inclusion of $K_{\rm th}$ and $\sigma_{\rm th}$ as free parameters by re-running our analysis for the benchmark model and the data sets with either only γ-ray detected pulsars or also including the unidentified sources. The scaling of the sensitivity map (exp ($K_{\rm th}$)) was fixed to 4 and 8, respectively. In addition we applied a hard cut-off (similar to $\sigma_{\rm th} \rightarrow 0$). Observed sources with fluxes smaller than the threshold were removed from the data set. The results obtained are consistent with the results presented in the paper.

Except for the analysis which also includes unidentified sources, the most important caveat of using the detection sensitivity from Abdo et al. (2013) is the absence association with a radio pulsar, the pulse frequency of which would subsequently be phase folded into the γ-ray analysis to detect pulsed γ-ray emission. Constructing a sensitivity map for the combined detection in γ-rays and radio would first of all require knowledge of the radio γ-ray correlation, which currently is ill constrained (e.g. Calore et al. 2016). In addition, the largest complication with adding information about the radio sensitivity is that most radio detections of pulsars come from deep pointing observations towards particular objects instead of surveys. As such, it is virtually impossible to construct a sensible radio sensitivity map similar as the one existing for gamma-rays. Finally, the detectability of the pulsed radio emission depends on the free-electron column density due to dispersive smearing and scatter broadening (e.g. Hessels et al. 2007; Calore et al. 2016). Since the free-electron density depends on both position and distance (Yao et al. 2017) this would make the sensitivity map inherently three-dimensional, and as such result in much larger computing times. The derivation of a representative radio–γ-ray correlation and the construction of a three-dimensional sensitivity map is beyond the scope of this work. The introduced spread of the sensitivity function, $\sigma_{\rm th}$, can capture in part that some of the less bright sources need not necessarily be detected. However, it is by no means a complete treatment of the uncertainty. In order to assess to what extent the absence of a dedicated sensitivity function including the detectability of radio pulsations systematically affects our results we also performed the analysis including unidentified sources. Since the results for data sets with and without unidentified γ-ray sources broadly agree we believe that our results do not suffer from a large systematic bias.

5 CONCLUSION

We have performed a Bayesian-unbinned likelihood analysis and – for the first time in this context – done Bayesian model comparison in order to constrain the properties of the Galactic population of γ-ray MSPs, self-consistently taking into account various sources of uncertainties. We used a sample of 96 γ-ray detected MSPs, but verified that our results remain similar under the inclusion of an additional 69 well-motivated MSP candidates. In order to deal with distance uncertainties we developed a novel method to construct PDFs for the distance to individual pulsars and the distance proxies. We use the YMW16 electron-density model to construct a PDF for the DM given the true distance to a pulsar by sampling from the model its 35 free parameters. We therefore take into account the uncertainties on the derived parameters within the electron density model (Yao et al. 2017). Distance and flux uncertainties were then marginalized over. The normalization and variance of the flux-detection threshold were treated as free parameters in our analysis. Results for different parametrizations of the luminosity function and spatial profile are compared by computing Bayes factors.

We find that a Lorimer-disc profile is preferred over a disc with a Gaussian radial profile, although the parameters are only loosely constrained. There is clear evidence for a turnover in the luminosity function, ruling out a single power-law parametrization (with hard or superexponential cut-off). Instead, both a broken power law and a lognormal function provide good fits to the luminosity function.

Our analysis suggests the presence of $\sim 2 \times 10^4$ MSPs in the Galactic disc. However, within uncertainties this number could be as large as $\sim 10^5$. These numbers are in agreement with the expected MSP population derived using radio catalogues (Cordes & Chernoff 1997; Lyne et al. 1998; Levin et al. 2013).

Contrary to previous claims (Hooper et al. 2013; Cholis, Hooper & Linden 2015; Hooper & Mohlabeng 2016), we find the MSP interpretation of the GCE to be fully compatible with the characteristics of the disc MSPs. Therefore, we agree with the findings of Yuan & Zhang (2014), Petrović et al. (2015), and Ploeg et al. (2017). Our characterization of the luminosity function and detection sensitivity suggest that if the luminosity function of the bulge MSP population is identical to that of the disc MPS, and if 100 per cent of the GCE is due to MSPs, only a handful of sources should have been detected from the bulge, whereas in the past larger numbers were suggested. We explicitly tested for the presence of a bulge component in our analysis, but find that we currently lack sensitivity to place interesting constraints on the bulge population of MSPs. In the future, an extension of the work by Saz Parkinson et al. (2016) or a dedicated analysis to characterize unassociated sources as likely pulsars (Ajello et al. 2017) can be potentially powerful methods to constrain the bulge population.

At the peak of the luminosity function we find a higher detection completeness than previous work (Winter et al. 2016). Consequently, our luminosity-per-stellar-mass ratio of $\sim 3 \times 10^{26}$ erg s^{-1} M$_\odot^{-1}$ is significantly smaller than what has been derived in other works (Winter et al. 2016; Eckner et al. 2017; Macias et al. 2018). It should be mentioned that the completeness suffers from considerable uncertainties due to its dependence on the detection sensitivity, spatial profile, and luminosity function.

The results presented in this work have direct implications for the detectability of a diffuse disc MSP component due to unresolved sources, their contribution to the isotropic γ-ray background (Faucher-Giguere & Loeb 2010; Siegal-Gaskins et al. 2011; Calore et al. 2014), the bulge-to-disc ratio of MSPs (Bartels et al. 2018; Macias et al. 2018), the expected emission from dwarf galaxies (Winter et al. 2016), and the detectability of MSPs in external Galaxies such as M31 (Eckner et al. 2017).

Although the properties of the galactic disc MSP population are the main topic of this paper, the methods we describe can be applied directly to any population of astrophysical sources where unassociated sources are present and distances uncertainties are large, a situation commonly found in population analyses.

ACKNOWLEDGEMENTS

We thank Jason Hessels, Sebastian Liem, and Dick Manchester for discussion, Dan Hooper, Pasquale Serpico, and Gabrijela Zaharijas for feedback on the manuscript, and David Smith and Toby Burnett for providing the sensitivity map. This work was carried out on the Dutch national e-infrastructure with the support of SURF Cooperative. This research is funded by the Netherlands Organisation for Scientific Research (NWO) through the VIDI research program

'Probing the Genesis of Dark Matter' (680-47-532; TE, CW) and through a GRAPPA-PhD fellowship (022.004.017; RB).

REFERENCES

Abazajian K. N., 2011, JCAP, 1103, 010
Abdo A. A. et al., 2009a, Science, 325, 848
Abdo A. A. et al., 2009b, ApJ, 699, 1171
Abdo A. A. et al., 2013, ApJS, 208, 17
Acero F. et al., 2015, ApJS, 218, 23
Ajello M. et al., 2017, preprint (arXiv:1705.00009)
Bartels R., Krishnamurthy S., Weniger C., 2016, Phys. Rev. Lett., 116, 051102
Bartels R., Storm E., Weniger C., Calore F., 2018 , Nat. Astron., (in press)
Bartels R., Hooper D., Linden T., Mishra-Sharma S., Rodd N. L., Safdi B. R., Slatyer T. R., 2018, Phys. Dark Univ., 20, 88
Bhattacharya D., van den Heuvel E. P. J., 1991, Phys. Rep., 203, 1
Buchner J. et al., 2014, A&A, 564, A125
Calore F., Di Mauro M., Donato F., 2014, ApJ, 796, 1
Calore F., Cholis I., Weniger C., 2015, JCAP, 1503, 038
Calore F., Di Mauro M., Donato F., Hessels J. W. T., Weniger C., 2016, ApJ, 827, 143
Caraveo P. A., 2014, Ann. Rev. Astron. Astrophys., 52, 211
Cholis I., Hooper D., Linden T., 2014, preprint (arXiv:1407.5583)
Cholis I., Hooper D., Linden T., 2015, JCAP, 1506, 043
Clark C. J. et al., 2018, Sci. Adv., 4, eaao7228
Cognard I. et al., 2011, ApJ, 732, 47lu
Cordes J. M., Chernoff D. F., 1997, ApJ, 482, 971
Cordes J. M., Lazio T. J. W., 2002, preprint (arXiv:astro-ph/0207156)
Daylan T., Finkbeiner D. P., Hooper D., Linden T., Portillo S. K. N., Rodd N. L., Slatyer T. R., 2016, Phys. Dark Univ., 12, 1
Eckner C. et al., 2017, ApJ, 862, 79
Faucher-Giguere C. A., Loeb A., 2010, JCAP, 1001, 005
Feroz F., Hobson M. P., Bridges M., 2009, MNRAS, 398, 1601
Goodenough L., Hooper D., 2009, preprint (arXiv:0910.2998)
Gordon C., Macias O., 2013, Phys. Rev., D88, 083521
Gorski K. M., Hivon E., Banday A. J., Wandelt B. D., Hansen F. K., Reinecke M., Bartelman M., 2005, ApJ, 622, 759
Grégoire T., Knödlseder J., 2013, A&A, 554, A62
Guillemot L. et al., 2013, ApJ, 768, 169
Hessels J. W. T., Ransom S. M., Stairs I. H., Kaspi V. M., Freire P. C. C., 2007, ApJ, 670, 363
Hobson M. P., Bridle S. L., Lahav O., 2002, MNRAS, 335, 377
Hooper D., Linden T., 2016, JCAP, 1608, 018
Hooper D., Mohlabeng G., 2016, JCAP, 1603, 049
Hooper D., Cholis I., Linden T., Siegal-Gaskins J., Slatyer T., 2013, Phys. Rev., D88, 083009
Kass R. E., Raftery A. E., 1995, J. Am. Stat. Assoc., 90, 773
Kuiper L., Hermsen W., Verbunt F., Thompson D. J., Stairs I. H., Lyne A. G., Strickman M. S., Cusumano G., 2000, A&A, 359, 615
Lee S. K., Lisanti M., Safdi B. R., Slatyer T. R., Xue W., 2016, Phys. Rev. Lett., 116, 051103
Levin L. et al., 2013, MNRAS, 434, 1387
Licquia T. C., Newman J. A., 2015, Astrophys. J., 806, 96
Lorimer D. R. et al., 2006, MNRAS, 372, 777
Lorimer D. R. et al., 2015, MNRAS, 450, 2185
Lorimer D. R., 2001, Living Rev. Rel., 4, 5
Lorimer D. R., 2003, Proc. IAU Symp. 218, Young Neutron Stars and Their Environment, Sydney, Australia
Lyne A. G. et al., 1998, MNRAS, 295, 743
Macias O., Gordon C., Crocker R. M., Coleman B., Paterson D., Horiuchi S., Pohl M., 2018, Nat. Astron., 2, 387
Manchester R. N., Hobbs G. B., Teoh A., Hobbs M., 2005, AJ, 129, 1993
McCann A., 2015, ApJ, 804, 86
Nolan P. L. et al., 2012, ApJS, 199, 31
Petrović J., Serpico P. D., Zaharijas G., 2015, JCAP, 1502, 023
Pletsch H. J. et al., 2012, Science, 338, 1314
Ploeg H., Gordon C., Crocker R., Macias O., 2017, JCAP, 1708, 015
Roberts M. S. E., 2011, in Burgay M., D'Amico N., Esposito P., Pellizzoni A., Possenti A., eds, AIP Conf. Proc. Vol. 1357, New Black Widows and Redbacks in the Galactic Field. Am. Inst. Phys., New York, p. 127
Sanpa-arsa S., 2016, PhD thesis. Univ. Virginia
Saz Parkinson P. M., Xu H., Yu P. L. H., Salvetti D., Marelli M., Falcone A. D., 2016, ApJ, 820, 8
Siegal-Gaskins J. M., Reesman R., Pavlidou V., Profumo S., Walker T. P., 2011, MNRAS, 415, 1074
Story S. A., Gonthier P. L., Harding A. K., 2007, ApJ, 671, 713
Taylor J. H., Cordes J. M., 1993, ApJ, 411, 674
Trotta R., 2008, Contemp. Phys., 49, 71
Verbiest J. P. W., Weisberg J. M., Chael A. A., Lee K. J., Lorimer D. R., 2012, ApJ, 755, 39
Wang P. et al., 2018, The Astronomer's Telegram, p. 11584
Winter M., Zaharijas G., Bechtol K., Vandenbroucke J., 2016, ApJ, 832, L6
Yao J. M., Manchester R. N., Wang N., 2017, ApJ, 835, 29
Yuan Q., Zhang B., 2014, JHEP, 3, 1

APPENDIX A: MILLISECOND PULSAR SAMPLE

In Table A1 we show the source list used in this work. The full list is available at http://github.com/tedwards2412/MSPDist. We separated the table in γ-ray detected pulsars and unassociated sources. For each source we give the position, γ-ray flux (0.1−100 GeV), DM, and/or parallax if available. Finally, the catalogues in which the sources appear are given.

Table A1. Millisecond pulsar sample separated into γ-ray detected MSPs and MSP candidates from Saz Parkinson et al. (2016) (see text for details). The different columns provide respectively: the name of the source, Galactic longitude, and latitude in degrees, γ-ray flux in the range 0.1−100 GeV, the DM and/or parallax from that ATNF (Manchester et al. 2005) if available, and finally a reference to the relevant catalogues.

Name	ℓ [deg]	b [deg]	Flux $[10^{-12}\,\mathrm{erg\,cm^{-2}\,s^{-1}}]$	DM $[\mathrm{cm^{-3}\,pc}]$	Parallax [mas]	Catalogues[a]
			γ-ray pulsars (96)			
J0023+0923	111.5	−52.9	7.28 ± 0.81	14.33	0.93 ± 0.16	1,2,3,4,5
J0030+0451	113.1	−57.6	60.68 ± 1.51	4.34	3.08 ± 0.09	1,2,3,4,5
J0034−0534	111.5	−68.1	18.04 ± 1.02	13.77	–	1,2,3,4,5
J0101−6422	301.2	−52.7	12.45 ± 0.85	11.93	–	1,2,3,4,5
J0102+4839	124.9	−14.2	16.76 ± 1.39	53.50	–	1,2,3,5
J0218+4232	139.5	−17.5	48.14 ± 1.80	61.25	0.16 ± 0.09	1,2,3,4,5
J0248+4230[f]	144.9	−15.3	5.21 ± 0.81	48.2	–	2,4,5
J0251+26	153.9	−29.5	6.87 ± 0.99	20.00	–	2,3,4,5
J0308+74[b]	131.7	14.2	14.57 ± 0.79	6.35	–	2,3,5
J0318+0253	178.4	−43.6	5.71 ± 0.74	26.	–	2,3,4,5
J0340+4130	153.8	−11.0	22.24 ± 1.33	49.59	0.7 ± 0.5	1,2,3,4,5
J0437−4715	253.4	−42.0	17.87 ± 0.88	2.64	6.37 ± 0.09	1,2,3,4,5
J0533+67	144.8	18.2	9.57 ± 0.89	57.40	–	2,3,5
J0605+37	174.2	8.0	6.88 ± 0.95	21.00	–	2,3,5
J0610−2100	227.7	−18.2	11.48 ± 1.07	60.67	–	1,2,3,4,5
J0613−0200	210.4	−9.3	33.57 ± 1.64	38.78	0.93 ± 0.2	1,2,3,4,5
J0614−3329	240.5	−21.8	110.80 ± 2.36	37.05	–	1,2,3,4,5
J0621+25	187.1	5.1	11.04 ± 1.50	83.60	–	2,3,4
J0737−3039A[c]	245.2	−4.5	4.00 ± 1.00	48.92	–	5
J0740+6620	149.7	29.6	4.77 ± 0.68	14.96	2.3 ± 0.7	2,4,5
J0751+1807	202.8	21.1	13.04 ± 0.97	30.25	0.82 ± 0.17	1,2,3,4,5
J0931−1902	251.0	23.0	3.00 ± 0.86	41.49	1.2 ± 0.9	2,4,5
J0955−61	283.7	−5.7	8.24 ± 1.27	160.70	–	2,5
J1012−4235	274.2	11.2	7.48 ± 1.12	71.60	–	2,3,4,5
J1023+0038	243.4	45.8	5.35 ± 0.97	14.32	0.731 ± 0.022	3,4
J1024−0719	251.7	40.5	3.58 ± 0.52	6.48	0.8 ± 0.3	1,2,3,4,5
J1035−6720[d]	290.4	−7.8	25.94 ± 1.47	84.16	–	2,3,4,5
J1036−8317	298.9	−21.5	5.78 ± 0.95	27.00	–	2,4,5
J1124−3653	284.1	22.8	13.16 ± 1.09	44.90	–	1,2,3,5
J1125−5825	291.8	2.6	14.51 ± 2.66	124.79	–	1,2,3,4,5
J1137+7528[e]	129.1	40.8	2.28 ± 0.59	29.1702	–	2,4,5
J1142+0119	267.6	59.4	6.24 ± 0.82	19.20	–	2,3,5
J1207−5050	295.9	11.4	7.89 ± 1.16	50.60	–	2,3,4,5
J1227−4853	299.0	13.8	41.36 ± 1.67	43.42	–	2,3,4,5
J1231−1411	295.5	48.4	102.86 ± 2.12	8.09	–	1,2,3,4,5
J1301+0833	310.8	71.3	10.63 ± 0.97	13.20	–	2,3,4,5
J1302−32	305.6	29.8	11.30 ± 1.13	26.20	–	2,3,5
J1311−3430	307.7	28.2	64.69 ± 1.89	37.84	–	2,3,4,5
J1312+0051	314.9	63.2	16.50 ± 1.10	15.30	–	2,3,5
J1431−4715	320.1	12.3	6.41 ± 0.95	59.35	–	4,5
J1446−4701	322.5	11.4	12.55 ± 1.30	55.83	–	1,2,3,4,5
J1455-3330	330.8	22.5	2.15 ± 0.50	13.57	0.99 ± 0.22	4,5
J1513−2550[e]	338.8	27.0	7.03 ± 0.98	46.86	–	2,3,4,5
J1514−4946	325.2	6.8	42.81 ± 2.12	31.05	–	1,2,3,4,5
J1536−4948	328.2	4.8	87.43 ± 3.05	38.00	–	2,3,5
J1543−5149	327.9	2.7	21.83 ± 2.60	50.93	–	2,4,5
J1544+4937	79.2	50.2	3.58 ± 0.64	23.23	–	2,4,5
J1552+5437	85.6	47.2	4.53 ± 0.64	22.90	–	2,4,5
J1600−3053	344.1	16.5	6.16 ± 1.07	52.33	0.5 ± 0.08	1,2,3,4,5
J1614−2230	352.6	20.2	23.37 ± 1.49	34.92	1.5 ± 0.1	1,2,3,4,5
J1622−0315[e]	10.8	30.7	10.15 ± 1.28	21.4	–	2,3,4,5
J1628−3205	347.4	11.5	12.12 ± 1.48	42.10	–	2,3,4,5

Table A1 – *continued*

Name	ℓ [deg]	b [deg]	Flux $[10^{-12}\,\mathrm{erg\,cm^{-2}\,s^{-1}}]$	DM $[\mathrm{cm^{-3}\,pc}]$	Parallax [mas]	Catalogues[a]
J1630+37	60.2	43.3	6.86 ± 1.01	14.10	–	2,3,5
J1640+2224	41.0	38.3	2.59 ± 0.45	18.46	0.66 ± 0.07	4,5
J1658−5324	334.9	− 6.6	20.32 ± 1.99	30.81	–	1,2,3,4,5
J1713+0747	28.8	25.2	9.41 ± 1.25	15.92	0.81 ± 0.03	1,2,3,4,5
J1730−2304	3.2	6.0	12.97 ± 2.38	9.62	1.19 ± 0.27	4,5
J1732−5049	340.0	− 9.4	8.52 ± 1.34	56.84	–	2,4,5
J1741+1351	37.9	21.6	5.68 ± 1.06	24.20	0.56 ± 0.13	1,2,3,4,5
J1744−1134	14.8	9.2	39.16 ± 2.18	3.14	2.53 ± 0.07	1,2,3,4,5
J1744−7619	317.1	− 22.5	22.50 ± 1.31	–	–	2,3,4,5
J1745+1017	34.9	19.3	10.56 ± 1.48	23.97	–	2,3,4,5
J1747−4036	350.2	− 6.4	15.97 ± 1.79	152.96	–	1,2,3,4,5
J1805+06	33.4	13.0	5.51 ± 0.99	65.00	–	2,3,4,5
J1810+1744	44.6	16.8	22.38 ± 1.37	39.70	–	1,2,3,4,5
J1811−2405	6.9	− 2.5	21.79 ± 4.30	60.60	–	2,4
J1816+4510	72.9	24.8	12.13 ± 0.93	38.89	–	2,3,4,5
J1832−0836	23.0	0.2	15.27 ± 2.99	28.19	–	4,5
J1843−1113	22.0	− 3.4	19.81 ± 2.80	59.96	0.69 ± 0.33	2,4,5
J1855−1436[e]	20.4	− 7.6	7.85 ± 1.00	109.2	–	4,5
J1858−2216	13.6	− 11.4	8.33 ± 1.09	26.60	–	1,2,3,5
J1902−5105	345.6	− 22.4	21.47 ± 1.16	36.25	–	1,2,3,4,5
J1902−70	324.4	− 26.5	12.28 ± 0.99	19.50	–	2,3,5
J1909+21	53.7	5.8	7.01 ± 1.10	62.00	–	4,5
J1921+0137[e]	37.8	− 5.9	15.92 ± 1.92	104.9	–	2,3,4,5
J1939+2134	57.5	− 0.3	9.18 ± 3.32	71.02	0.22 ± 0.08	1,4,5
J1946−5403	343.9	− 29.6	11.29 ± 0.92	23.70	–	2,3,4,5
J1959+2048	59.2	− 4.7	17.91 ± 1.54	29.12	–	1,2,3,4,5
J2017+0603	48.6	− 16.0	34.97 ± 1.69	23.92	0.4 ± 0.3	1,2,3,4,5
J2017−1614[e]	27.3	− 26.2	10.40 ± 1.20	25.4380	–	2,3,4,5
J2042+0246[e]	49.0	− 23.0	3.61 ± 0.55	9.2694	–	2,4,5
J2043+1711	61.9	− 15.3	30.22 ± 1.41	20.76	0.64 ± 0.08	1,2,3,4,5
J2047+1053	57.1	− 19.6	3.56 ± 0.58	34.60	–	1,2,3,5
J2051−0827	39.2	− 30.5	3.18 ± 0.52	20.73	–	1,2,4,5
J2052+1218	59.1	− 20.0	6.53 ± 1.04	42.00	–	2,4,5
J2124−3358	10.9	− 45.4	39.40 ± 1.39	4.60	2.4 ± 0.4	1,2,3,4,5
J2129−0429	48.9	− 36.9	10.50 ± 1.06	16.90	–	2,3,4,5
J2205+6015[f]	103.7	3.8	7.50 ± 1.52	157.6	–	4,5
J2214+3000	86.9	− 21.7	33.00 ± 1.24	22.55	2.3 ± 0.7	1,2,3,4,5
J2215+5135	99.9	− 4.2	13.75 ± 1.14	69.20	–	1,2,3,4,5
J2234+0944	76.3	− 40.4	8.28 ± 1.01	17.8	1.3 ± 0.5	2,3,4,5
J2241−5236	337.4	− 54.9	30.97 ± 1.22	11.41	–	1,2,3,4,5
J2256−1024	59.2	− 58.2	7.66 ± 0.78	13.80	–	2,3,4,5
J2302+4442	103.4	− 14.0	38.10 ± 1.40	13.73	–	1,2,3,4,5
J2310−0555[e]	69.7	− 57.9	3.48 ± 0.56	15.5139	–	2,4,5
J2339−0533[e]	81.3	− 62.5	30.06 ± 1.39	8.72	–	2,3,4,5
			Other sources (69)			
J0039.3+6256	121.6	0.1	9.11 ± 1.14	–	–	2,3,4
J0212.1+5320	134.9	− 7.6	17.14 ± 1.56	–	–	2,3,4
J0238.0+5237	138.8	− 6.9	11.60 ± 1.21	–	–	2,3,4
J0312.1−0921	191.5	− 52.4	5.23 ± 0.84	–	–	2,3,4
J0336.1+7500	133.1	15.5	9.97 ± 1.04	–	–	2,3,4
J0401.4+2109	171.4	− 23.3	6.27 ± 1.09	–	–	3,4
J0523.3−2528	228.2	− 29.8	19.91 ± 1.24	–	–	2,3,4
J0542.5−0907c	213.4	− 19.4	13.64 ± 1.81	–	–	3,4
J0545.6+6019	152.5	15.7	7.87 ± 0.95	–	–	2,3,4
J0737.2−3233	246.8	− 5.5	13.83 ± 1.52	–	–	2,3,4
J0744.1−2523	241.3	− 0.7	23.86 ± 1.78	–	–	2,3,4
J0744.8−4028	254.6	− 8.0	9.40 ± 1.36	–	–	3,4
J0758.6−1451	234.0	7.6	7.30 ± 1.06	–	–	2,3,4
J0802.3−5610	269.9	− 13.2	13.01 ± 1.18	–	–	2,3,4
J0826.3−5056	267.4	− 7.4	10.66 ± 1.59	–	–	3,4
J0838.8−2829	250.6	7.8	12.74 ± 1.20	–	–	2,3,4
J0933.9−6232	282.2	− 7.9	12.27 ± 1.06	–	–	2,3,4

Table A1 – *continued*

Name	ℓ [deg]	b [deg]	Flux $[10^{-12}\ \mathrm{erg\,cm^{-2}\,s^{-1}}]$	DM $[\mathrm{cm^{-3}\,pc}]$	Parallax [mas]	Catalogues[a]
J0953.7−1510	251.9	29.6	5.85 ± 0.71	–	–	2,3,4
J0954.8−3948	269.8	11.5	18.29 ± 1.23	–	–	2,3,4
J0957.6+5523	158.6	47.9	95.86 ± 2.73	–	–	2,3,4
J1119.9−2204	276.5	36.1	16.85 ± 1.03	–	–	2,3,4
J1136.1−7411	297.8	− 12.1	11.18 ± 1.18	–	–	2,3,4
J1207.6−4537	295.0	16.6	4.17 ± 0.93	–	–	3,4
J1208.0−6901	299.0	− 6.5	7.50 ± 1.25	–	–	3,4
J1225.9+2953	185.2	83.8	8.70 ± 0.97	–	–	2,3
J1306.4−6043	304.8	2.1	35.12 ± 2.50	–	–	2,3,4
J1325.2−5411	307.9	8.4	10.75 ± 1.65	–	–	2,3,4
J1329.8−6109	307.6	1.4	16.47 ± 2.39	–	–	2,3,4
J1400.2−2413	322.4	36.0	5.82 ± 0.99	–	–	2,3,4
J1400.5−1437	326.9	45.0	9.36 ± 1.09	4.93	3.6 ± 1.1	2,3,4
J1412.3−6635	310.9	− 5.0	8.21 ± 1.46	–	–	3,4
J1458.7−2120	338.6	32.6	7.05 ± 1.05	–	–	2,3,4
J1539.2−3324	338.8	17.5	11.56 ± 1.03	–	–	2,3,4
J1544.6−1125	356.2	33.0	13.54 ± 1.40	–	–	2,3,4
J1600.3−5810	325.8	− 3.9	5.50 ± 1.40	–	–	3,4
J1616.8−5343	330.5	− 2.2	26.48 ± 2.62	–	–	2,3,4
J1624.2−3957	341.1	6.6	13.09 ± 2.53	–	–	3,4
J1625.1−0021	13.9	31.8	18.38 ± 1.26	–	–	2,3,4
J1630.2−1052	4.9	24.8	6.71 ± 1.32	–	–	2,3,4
J1641.5−5319	333.3	− 4.6	18.42 ± 2.24	–	–	2,3,4
J1653.6−0158	16.6	24.9	33.71 ± 1.83	–	–	2,3,4
J1702.8−5656	332.4	− 9.2	32.04 ± 1.66	–	–	2,3,4
J1717.6−5802	332.6	− 11.5	12.39 ± 1.30	–	–	2,3,4
J1722.7−0415	18.5	17.5	12.33 ± 2.08	–	–	2,3,4
J1730.6−0357	19.8	16.0	6.44 ± 1.25	–	–	2,3,4
J1740.5−2642	1.3	2.1	16.77 ± 2.51	–	–	3,4
J1743.9−1310	13.3	8.5	8.23 ± 1.79	–	–	3,4
J1748.5−3912	351.5	− 5.8	16.26 ± 1.94	–	–	3,4
J1749.7−0305	23.0	12.2	12.84 ± 1.88	–	–	3,4
J1753.6−4447	347.1	− 9.4	9.36 ± 1.28	–	–	2,3,4
J1759.2−3848	352.9	− 7.4	8.92 ± 1.69	–	–	2,3,4
J1808.3-3357	358.1	− 6.7	8.72 ± 1.44	–	–	2,3,4
J1823.2−4722	347.1	− 15.2	4.82 ± 1.01	–	–	3,4
J1827.7+1141	40.8	10.5	7.57 ± 1.31	–	–	2,3,4
J1830.8−3136	2.4	− 9.8	6.77 ± 1.35	–	–	2,3,4
J1908.8−0130	33.6	− 4.6	7.12 ± 0.94	–	–	2,3,4
J1918.2−4110	356.8	− 22.2	21.61 ± 1.86	–	–	2,3,4
J1950.2+1215	50.7	− 7.1	16.13 ± 1.75	–	–	2,3,4
J2004.4+3338	70.7	1.2	43.07 ± 2.79	–	–	2,3,4
J2006.6+0150	43.4	− 15.8	4.17 ± 1.02	–	–	3,4
J2026.8+2813	68.8	− 5.8	7.66 ± 1.50	–	–	3,4
J2035.0+3634	76.6	− 2.3	12.32 ± 1.82	–	–	2,3,4
J2039.6−5618	341.2	− 37.2	17.11 ± 1.38	–	–	2,3,4
J2043.8−4801	351.7	− 38.3	7.35 ± 0.93	–	–	2,3,4
J2112.5−3044	14.9	− 42.4	19.01 ± 1.39	–	–	2,3,4
J2117.6+3725	82.8	− 8.3	12.76 ± 1.31	–	–	2,3,4
J2133.0−6433	328.7	− 41.3	3.97 ± 0.67	–	–	2,3,4
J2212.5+0703	68.7	− 38.6	9.03 ± 1.03	–	–	2,3,4
J2250.6+3308	95.7	− 23.3	5.27 ± 0.87	–	–	3,4

[a](1) in 2PC (Abdo et al. 2013); (2) in 2FGL (Nolan et al. 2012); (3) in 3FGL (Acero et al. 2015); (4) in FL8Y https://fermi.gsfc.nasa.gov/ssc/data/access/lat/fl8y/; (5) in the Public list of Fermi–LAT detected γ–ray pulsars https://confluence.slac.stanford.edu/display/GLAMCOG/Public+List+of+LAT-Detected+Gamma-Ray+Pulsars.
[b]DM from Wang et al. (2018).
[c]γ-ray flux from Guillemot et al. (2013).
[d]DM from Clark et al. (2018).
[e]DM from Sanpa-arsa (2016).
[f]DM from http://astro.phys.wvu.edu/GalacticMSPs/GalacticMSPs.txt (compiled by Duncan Lorimer).

APPENDIX B: COORDINATE TRANSFORMATION

B1 Disc profile

The number density of MSPs in the disc is parametrized by a cylindrically symmetric profile. However, observations of MSPs only provide a location on the sky and sometimes distance information. In order to test a particular spatial profile against observations it is useful to convert the number density distribution of MSPs into a probability of finding a source at Galactic coordinates (ℓ, b) and at a particular distance D, $P(\ell, b, D)$ (this function is differential in ℓ, b and D, and normalized to one).

The disc profile is centred on the Galactic centre. As a first step, it is useful to convert the cylindrical coordinates into Cartesian coordinates, with the Galactic centre at origin

$$\begin{aligned} x_{\rm GC}(r, z, \theta) &= r\cos\theta \\ y_{\rm GC}(r, z, \theta) &= r\sin\theta \\ z_{\rm GC}(r, z, \theta) &= z. \end{aligned} \tag{B1}$$

We define the Sun to be at ($x_{\rm GC}$, $y_{\rm GC}$, $z_{\rm GC}$) = ($r_\odot$, 0, 0). A simple translation suffices to move the sun to the origin. We refer to this heliocentric-coordinate system with (x, y, z). The coordinate system with (ℓ, b, D) is related to the Cartesian coordinates through

$$\begin{aligned} x_{\rm GC}(\ell, b, D) &= r_\odot - D\cos(\ell)\cos(b) \\ y_{\rm GC}(\ell, b, D) &= D\sin(\ell)\cos(b) \\ z_{\rm GC}(b, D) &= D\sin(b). \end{aligned} \tag{B2}$$

With this information we can calculate the relevant Jacobians to perform the coordinate transformation, which for simplicity we perform in two steps to obtain

$$P(\ell, b, D) = \overbrace{\left|\frac{\partial(x, y, z)}{\partial(\ell, b, D)}\right|}^{=D^2\cos(b)}\overbrace{\left|\frac{\partial(r, z, \theta)}{\partial(x, y, z)}\right|}^{=1/r} P(r, z, \theta). \tag{B3}$$

Note that the Jacobian for the transformation of cylindrical to Cartesian coordinates cancels the presence of the same term in $P(r, z, \theta)$ described in the main text, Section 2.1.2.

B2 Bulge profile

The coordinate transformation for the bulge profile is analogous to that of the disc described in Section B1, with the only difference that we now start from spherical instead of cylindrical coordinates. In this case,

$$\left|\frac{\partial(r, \theta, \phi)}{\partial(x, y, z)}\right| = r^{-1}\sin^{-1}\phi. \tag{B4}$$

APPENDIX C: DETAILS ABOUT MODEL LIKELIHOODS

C1 Derivation of the likelihood function

We start with Bayes rule (e.g. Trotta 2008) with $\boldsymbol{\Theta}$ being our parameters of interest,

$$P(\boldsymbol{\Theta}|\mathcal{D}) \propto \mathcal{L}(\mathcal{D}|\boldsymbol{\Theta})\pi(\boldsymbol{\Theta}), \tag{C1}$$

where the posterior on the left-hand side is understood to be normalized to one w.r.t. $\boldsymbol{\Theta}$. Next, we introduce the unbinned likelihood

$$\mathcal{L}(\mathcal{D}|\boldsymbol{\Theta}) = e^{-\mu(\boldsymbol{\Theta})}\prod_{k=1}^{3} P(\mathcal{D}_k|\boldsymbol{\Theta}). \tag{C2}$$

The product arises because we have three independent data sets (e.g. Hobson, Bridle & Lahav 2002), for sources with parallax measurements, sources with DMs, and sources without measurement of a distance proxy. Let us next focus on the case where we have a distance measurement, denoted by κ, through either parallax or DM. Also, let us make explicit the dependence of the measured values of the distance proxy and flux on the true distance, flux, and their uncertainties (D, σ_κ, F, and σ_F). We note that measured spatial positions are assumed to correspond to the true values in this work. For a single pulsar, denoted by subscript i, we can use conditional probabilities to write

$$\begin{aligned} P(\ell_i, b_i, F_i, \kappa_i|\boldsymbol{\Theta}, D, \sigma_\kappa, F, \sigma_F) &= P(\ell_i, b_i|\boldsymbol{\Theta})P(F_i|F, \sigma_F)P(\kappa_i|D, \sigma_\kappa) \\ P(\ell_i, b_i, F_i, \kappa_i|\boldsymbol{\Theta}, \sigma_\kappa, \sigma_F) &= \int dF\,dD\,P(\ell_i, b_i, D, F|\boldsymbol{\Theta})P(F_i|F, \sigma_F)P(\kappa_i|D, \sigma_\kappa) \\ &= 4\pi\int dF\,dD\,D^2 P(\ell_i, b_i, D|\boldsymbol{\Theta})P(L = 4\pi D^2 F|\boldsymbol{\Theta})P(F_i|F, \sigma_F)P(\kappa_i|D, \sigma_\kappa). \end{aligned} \tag{C3}$$

In the second line we dropped any dependencies on the the spatial position; however, this can be thought of as being included in the uncertainties (σ_κ, σ_F). In reality the uncertainties can be a complicated function of the true flux, true distance and spatial position. Introducing these dependencies are beyond the scope of this work. In practice, we took the uncertainties from the observations, which will implicitly depend on spatial position, distance, and/or flux. In the second line we also made use of $P(A) = \int P(A, B)dB$ in order to integrate over distance and flux uncertainties. Finally, in the third line we changed variables from flux to luminosity. Since luminosity and spatial position are independent we can write $P(\ell, b, D, L) = P(\ell, b, D)P(L)$. This reproduces the likelihood in equation (4) without the flux threshold which is independent of the above discussion.

C2 Luminosity function measurement error

In Fig. 3 we show the best-fitting luminosity function for our benchmark model and compare it to observations. The data points are expectation values for each bin taking into account the uncertainty in the distance to the sources and on the flux. A description on how to compute the expectation values is given below. We emphasize that this approach is *not* used for the purpose of statistical inference, but *only* for the purpose of facilitating a visual comparison between predicted and measured luminosity functions in Fig. 3.

Let us again denote the true luminosity and flux of, and distance to, a particular pulsar by L, F, and D and measurements with subscript i. In this case we have for pulsars with a distance proxy (κ_i)

$$\begin{aligned} P(L|F_i, \kappa_i, \ell, b, \boldsymbol{\Theta}) &= \int \mathrm{d}F\mathrm{d}D\, P(L, D, F|F_i, \kappa_i, \ell, b, \boldsymbol{\Theta}) \\ &= \int \mathrm{d}F\mathrm{d}D\, P(L|D, F)P(F|F_i, \ell, b)P(D|\kappa_i, \ell, b, \boldsymbol{\Theta})\,. \end{aligned} \tag{C4}$$

Here $P(L|D, F) = \delta(L - 4\pi D^2 F)$. $P(F|F_i)$ is a Gaussian similar to that described in Section 2.1.4, but with the true and observed distance interchanged. The probability of a true distance given the observation is given by equation (6) in Verbiest et al. (2012) in case of a parallax measurement. When only a DM is available we derive $P(D|\kappa_i)$ using a Monte Carlo similar to the one described in Section 2.2.2, but this time obtaining the distance by sampling from 10^4 random realizations of the YMW16 model with the DM set equal to the measured value. Finally, when neither parallax nor distance information is present we use $P(D|\ell, b, \boldsymbol{\Theta})$ as given in Section 2.1.2. We then obtain the expectation value in a particular bin ($L_- \leq L < L_+$) through

$$P\,(L_- \leq L < L_+|F_i, \kappa_i, \ell, b) = \int_{L_- \leq 4\pi D^2 F}^{4\pi D^2 F < L_+} \mathrm{d}F\mathrm{d}D\, P(F|F_i, \ell, b)P(D|\kappa_i, \ell, b). \tag{C5}$$

Contributions from all pulsars are summed to obtain the overall expectation. Although the expectations in general are not integers, errors are treated as Poissonian and so the errorbars correspond to the square-root of the expectation.

APPENDIX D: RESULTS FOR DIFFERENT MODELS

In this section, we show corner plots similar to Fig. 2 for a selection of different models considered in the main text. Only changes with respect to the benchmark model are mentioned. In Fig. D1 we show the result for the model with a lognormal luminosity function. Fig. D2 contains the results for a model with a Gaussian disc profile. The results for a model including a bulge component is displayed in Fig. D3. Finally, we show the results obtained when using a pulsar sample consisting only of the 2PC MSPs (Fig. D4) and with the addition of unassociated sources (Fig. D5).

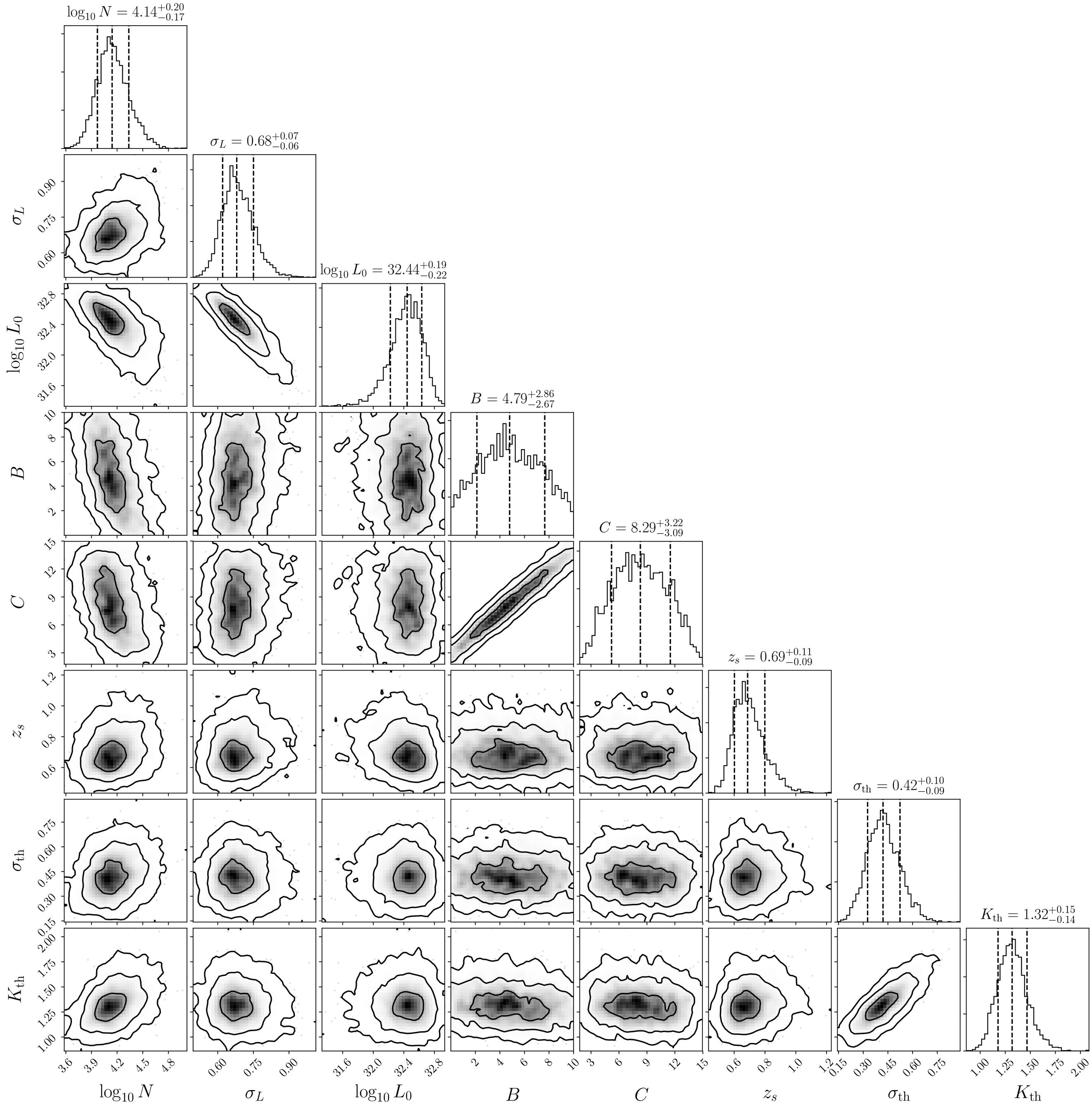

Figure D1. Similar to Fig. 2, but for the lognormal luminosity function.

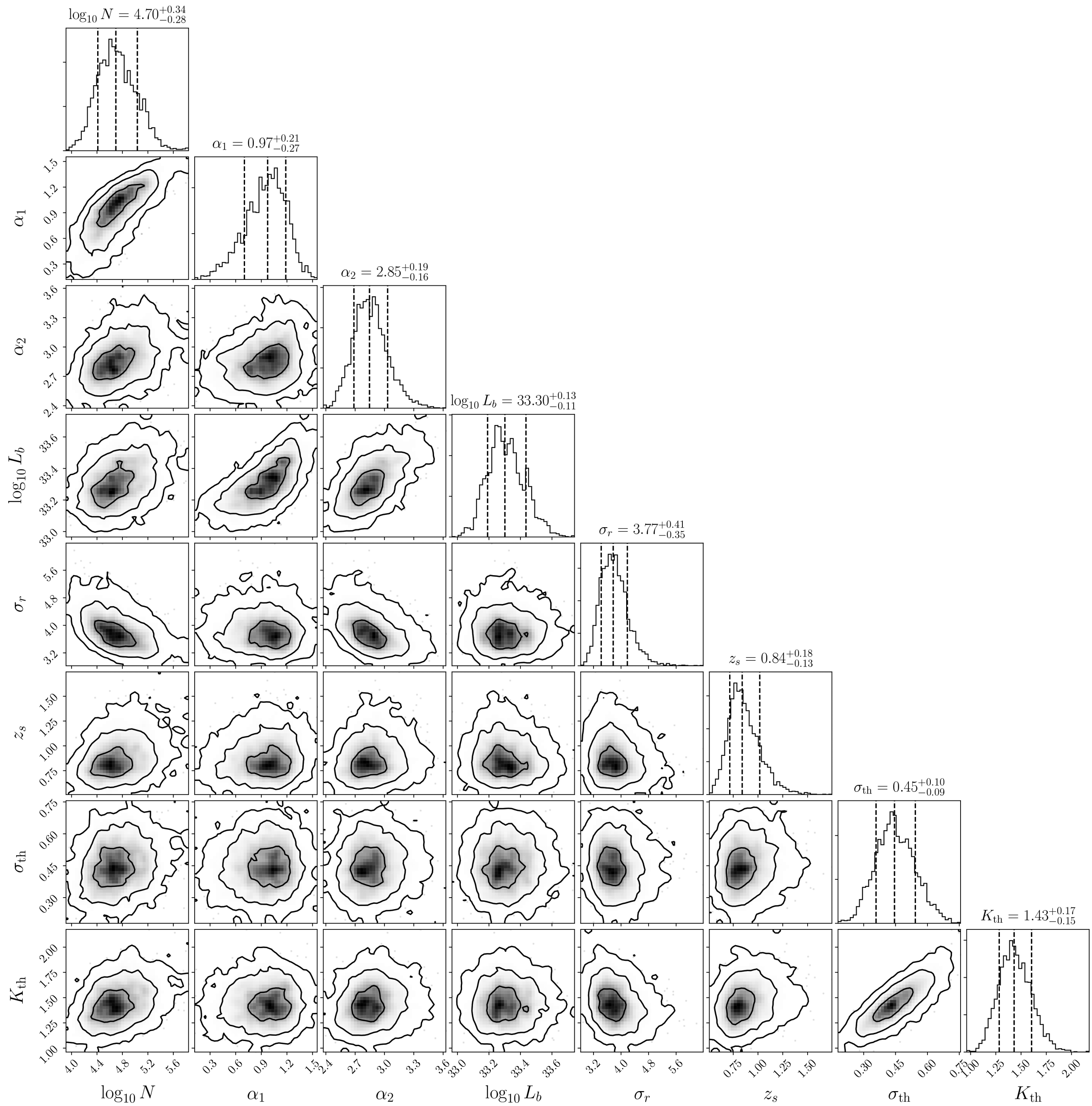

Figure D2. Similar to Fig. 2, but using a Gaussian radial profile for the disc.

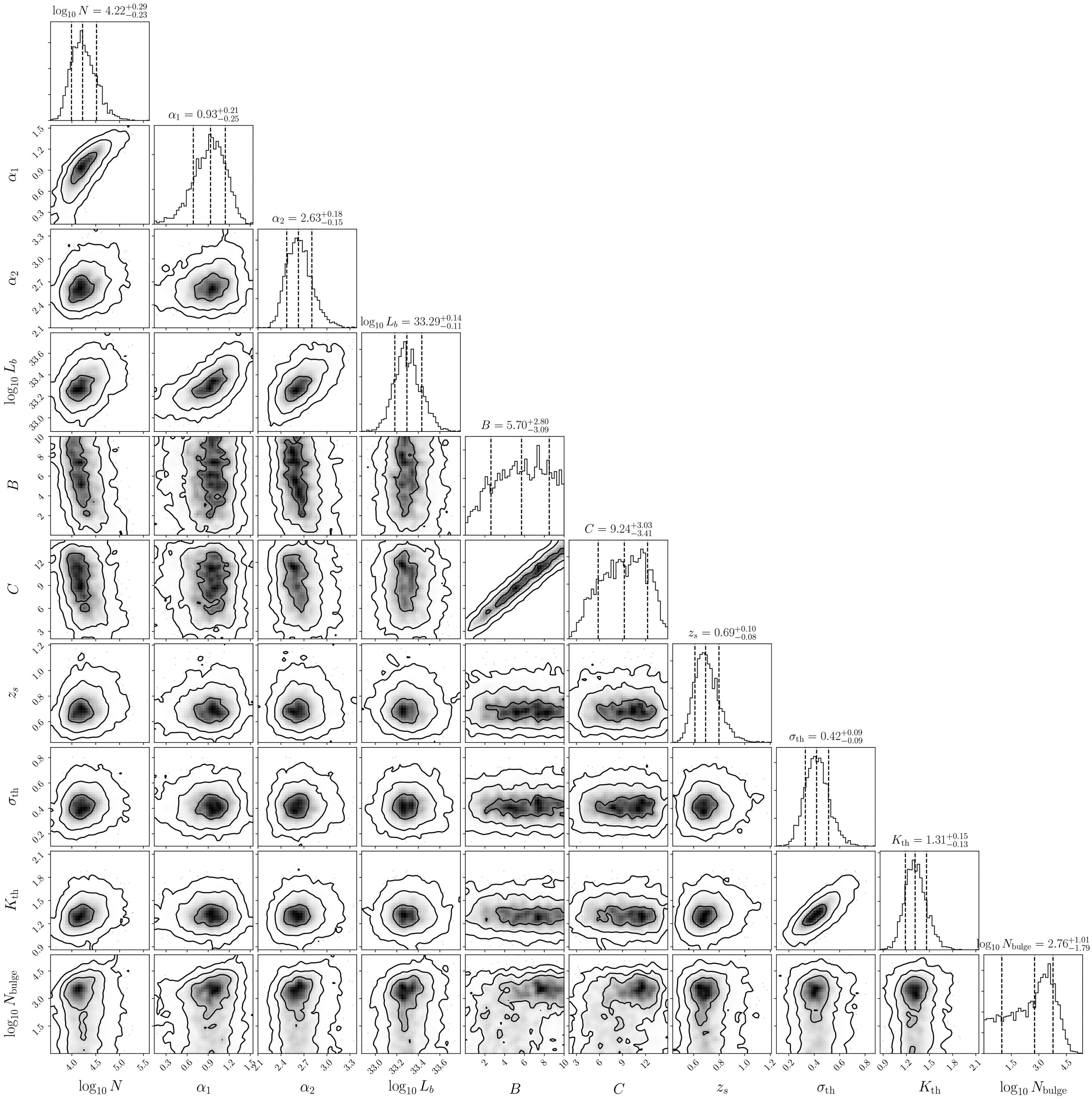

Figure D3. Similar to Fig. 2, but including an additional bulge component in the centre with an identical luminosity function.

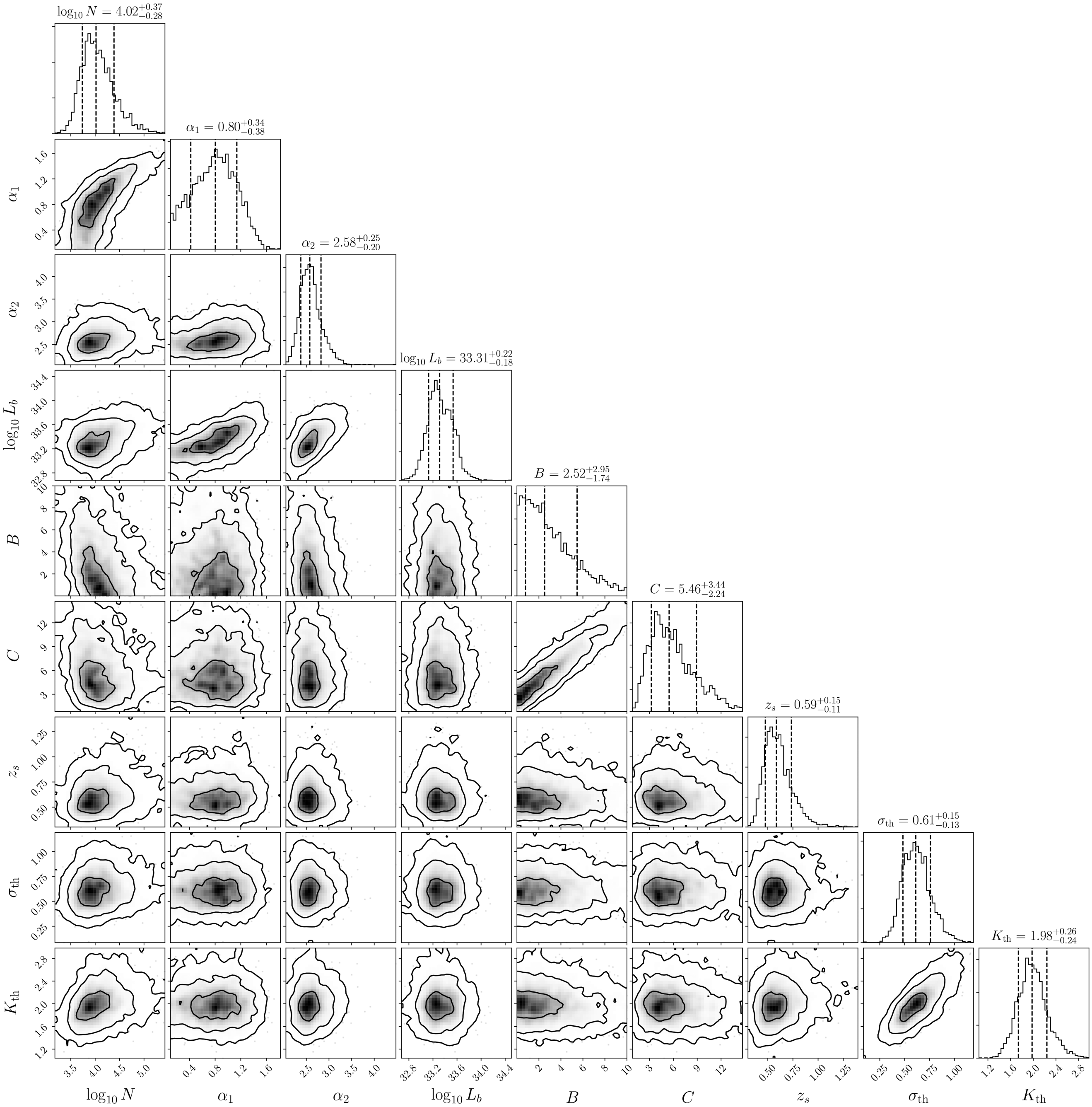

Figure D4. Similar to Fig. 2, but using a smaller data set based on the MSPs in the 2PC (Abdo et al. 2013).

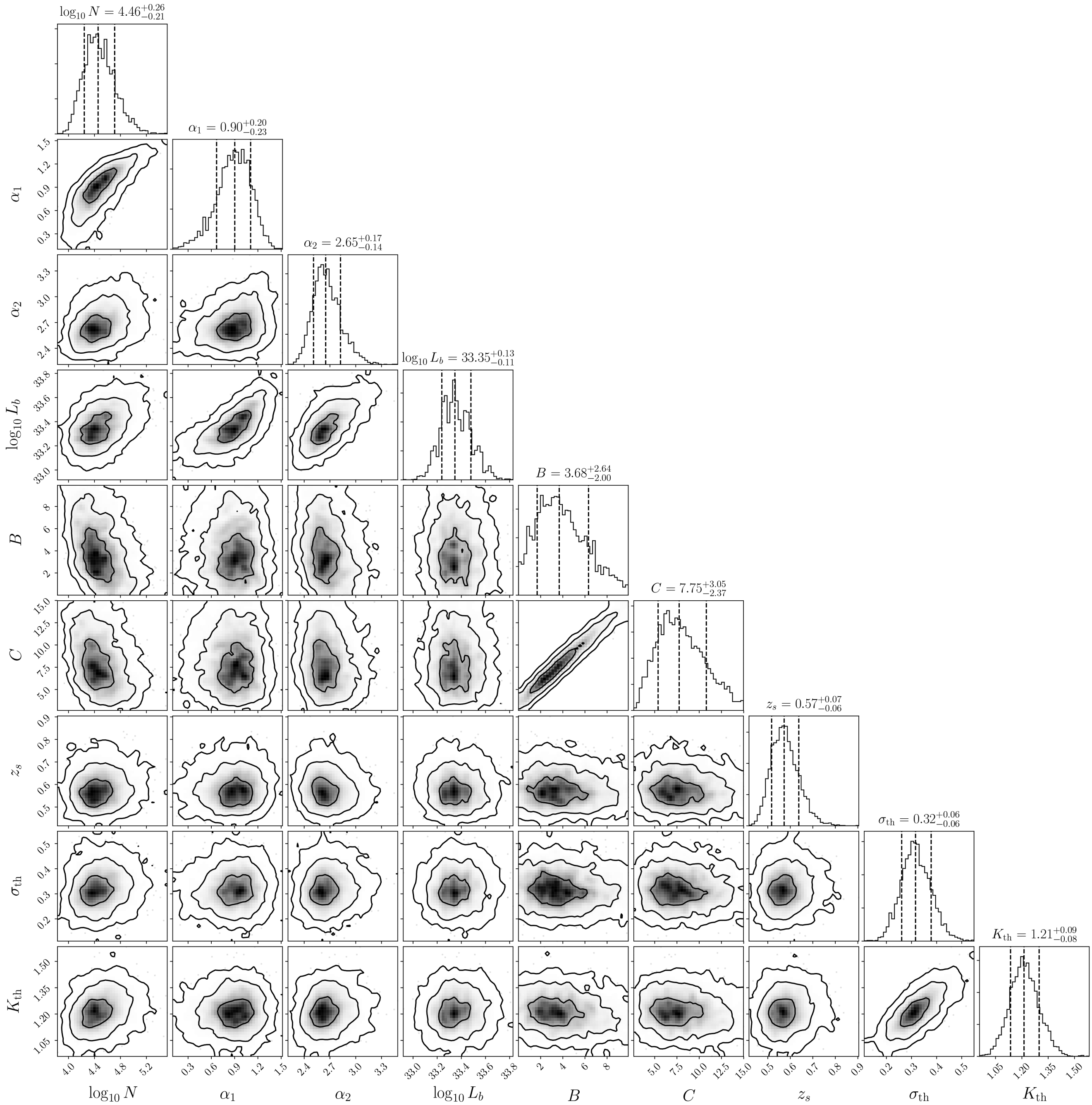

Figure D5. Similar to Fig. 2, but using a larger source sample including unassociated sources selected from Saz Parkinson et al. (2016).

This paper has been typeset from a TEX/LATEX file prepared by the author.